Theses and Dissertations

Spring 2013

Quantitative assessment of scatter correction techniques incorporated in next generation dual-source computed tomography

Sean David Mobberley
University of Iowa

Recommended Citation

QUANTITATIVE ASSESSMENT OF SCATTER CORRECTION

TECHNIQUES INCORPORATED IN NEXT GENERATION DUAL-

SOURCE COMPUTED TOMOGRAPHY

by

Sean David Mobberley

A thesis submitted in partial fulfillment
of the requirements for the Master of
Science degree in Biomedical Engineering
in the Graduate College of
The University of Iowa

May 2013

Thesis Supervisor: Professor Eric A. Hoffman

Graduate College
The University of Iowa
Iowa City, Iowa

CERTIFICATE OF APPROVAL

_____

MASTER'S THESIS

_____

This is to certify that the Master's thesis of

Sean David Mobberley

has been approved by the Examining Committee
for the thesis requirement for the Master of Science
degree in Biomedical Engineering at the May 2013 graduation.

Thesis Committee: _____

Eric A. Hoffman, Thesis Supervisor

_____

Joseph M. Reinhardt

_____

John D. Newell

ACKNOWLEDGMENTS

ABSTRACT

CT has emerged as a powerful method for imaging of the lung due to its widespread availability, high spatial resolution, high signal to noise ratio for lung tissue, and fast acquisition speed. Dual-source CT (DSCT) imaging can now provide anatomical, functional, and quantitative information about the lung. CT technology has rapidly evolved from its introduction in the medical field in the early 1970s, and its development through the decades has produced a profound change in the role of diagnostic imaging in medicine.

Accurate, cross-scanner assessment of in-vivo air density used to quantitatively assess amount and distribution of emphysema in COPD subjects has remained elusive. Hounsfield units (HU) within tracheal air can be considerably more positive than -1000 HU. With the advent of new dual-source scanners which employ dedicated scatter correction techniques, it is of interest to evaluate how the quantitative measures of lung density compare between dual-source and single-source scan modes. This study has sought to characterize in-vivo and phantom-based air metrics using dual-energy computed tomography technology where the nature of the technology has required adjustments to scatter correction.

Anesthetized ovine (N=6), swine (N=13: more human-like rib cage shape), lung phantom and a thoracic phantom were studied using a dual-source MDCT scanner (Siemens Definition Flash. Multiple dual-source dual-energy (DSDE) and single-source (SS) scans taken at different energy levels and scan settings were acquired for direct quantitative comparison. Density histograms were evaluated for the lung, tracheal, water and blood segments. Image data were obtained at 80, 100, 120, and 140 kVp in the SS

mode (B35f kernel) and at 80, 100, 140, and 140-Sn (tin filtered) kVp in the DSDE mode (B35f and D30f kernels), in addition to variations in dose, rotation time, and pitch. To minimize the effect of cross-scatter, the phantom scans in the DSDE mode was obtained by reducing the tube current of one of the tubes to its minimum (near zero) value.

When using image data obtained in the DSDE mode, the median HU values in the tracheal regions of all animals and the phantom were consistently closer to -1000 HU regardless of reconstruction kernel (chapter 3). Similarly, HU values of water and blood were consistently closer to their nominal values of 0 HU and 55 HU respectively. When using image data obtained in the SS mode the air CT numbers demonstrated a consistent positive shift of up to 35 HU with respect to the nominal -1000 HU value. In vivo data demonstrated considerable variability in tracheal, influenced by local anatomy with SS mode scanning while tracheal air was more consistent with DSDE imaging. Scatter effects in the lung parenchyma differed from adjacent tracheal measures.

In summary, data suggest that enhanced scatter correction serves to provide more accurate CT lung density measures sought to quantitatively assess the presence and distribution of emphysema in COPD subjects. Data further suggest that CT images, acquired without adequate scatter correction, cannot be corrected by linear algorithms given the variability in tracheal air HU values and the independent scatter effects on lung parenchyma.

TABLE OF CONTENTS

LIST OF TABLES

LIST OF FIGURES

CHAPTER 1: INTRODUCTION

Quantitative computed tomography (QCT) has emerged as a powerful tool in the assessment of disease states and injury through the extraction of quantifiable features in volumetric datasets. These extracted features provide a set of objective biomarkers which can be used as a means to quantify the severity, extent, status of disease, or normalcy of a condition under analysis, and to deliver a more accurate, patient centric treatment plan.

QCT is commonly used for cardiac calcium scoring, ossifications and bone-density measurements (1, 2), and accurate CT numbers are a requirement for mapping water content in the brain (3), quantifying abdominal fat (4), in the evaluation of the liver (5), and tracking tumor growth (6). In the chest, CT measures have included airway and parenchymal density based biomarkers (7, 8), which has been used in the classification of chronic respiratory disease, such as asthma and chronic obstructive pulmonary disease (COPD), which includes emphasema.

COPD is an advanced condition affecting estimated 8% of the population of the United States (9), and is globally the third leading cause of death after ischemic heart disease and stroke (10). The disease, particularly in its early stages, is underdiagnosed, with estimates of approximately half of those who have the disease in the United States are currently undiagnosed (11). An increased awareness among physicians of the prevalence of mild COPD and additional screening for and diagnosing the disease is important in reducing disability-adjusted life years (DALYs) lost due to the condition (12, 13).

The current standard method for diagnosing and classifying the stage of COPD is the global initiative for chronic obstructive lung disease's GOLD method which assesses the symptoms, degree of airflow limitation using spirometry, risk of exacerbations, and comorbidities separately and then combines the assessments in a rubric to grade the risk of future events (exacerbations, hospitalization, death). However, these assessments are largely subjective and often fail to accurately classify patients according to disease severity and subtype (14).

With the advancement of QCT imaging techniques, which can produce objective, quantifiable measures to assess the presence, severity and development of pathologies, new large multi-center longitudinal studies were created. The COPD genetic epidemiology (COPDGene) study was designed to identify those patients with increased genetic risk of developing COPD and track the progression of the disease (15). COPDGene subjects undergo QCT scans at total lung capacity (TLC) and at the end of a normal expiration (functional residual capacity, or FRC), with emphysema-like low-attenuation areas, being defined as the percent of the lung volume falling below a CT densitometry threshold (**Fig. 1** and **Fig. 2**), which is close to the value of air, on an inspiratory scan (16). Similarly, the severe asthma research program (SARP) study of air-trapping asthmatic phenotypes relies on the accurate CT measurement of air in the thorax, by defining individuals with more than 9.66% of their total lung volume at FRC at below a quantitative CT densitometry threshold as having air-trappings (**Fig. 3**) (17).

The accurate quantification of CT data is an essential element in the assessment of emphysema (in inspiratory scans) and in air trappings (in expiratory scans). Unfortunately, variability of intrathoracic air measurements limits accuracy of

emphysema and air trapping quantification, and this can make comparison between CT scanner make and models difficult. With the advent of new dual source scanners, quantitative accuracy must be verified by comparing results against traditional single source scans to ensure validity prior to being used in multi-center longitudinal studies.
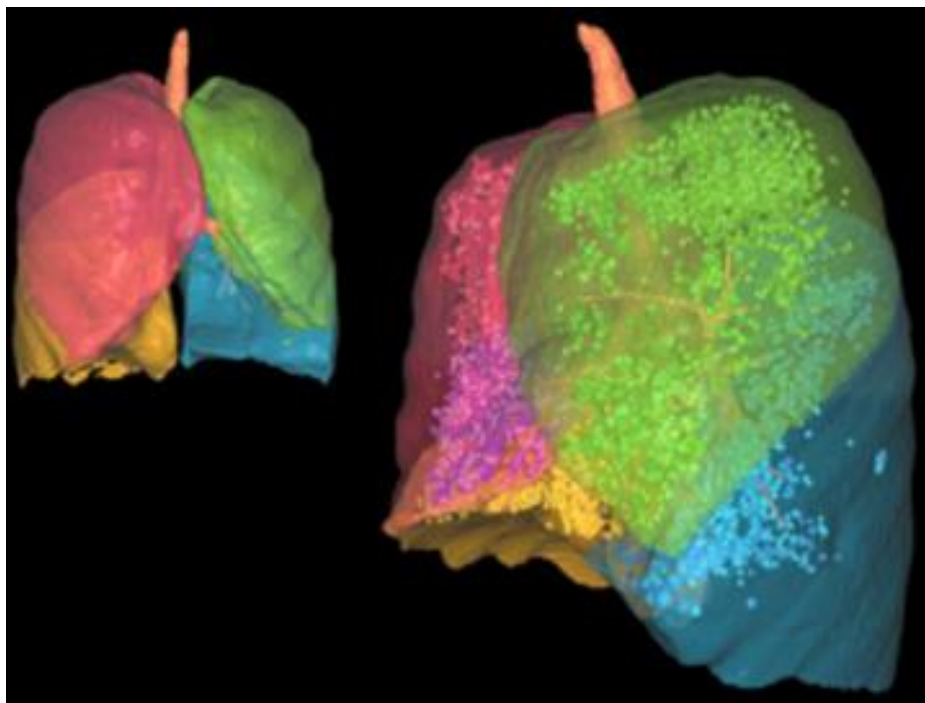
Figure 1. A volume-rendered image illustrating normal (*left set of lungs*) and emphysema-like regions (*small pockets of air, right set of lungs*) which are characterized in QCT by regions below -950 HU.
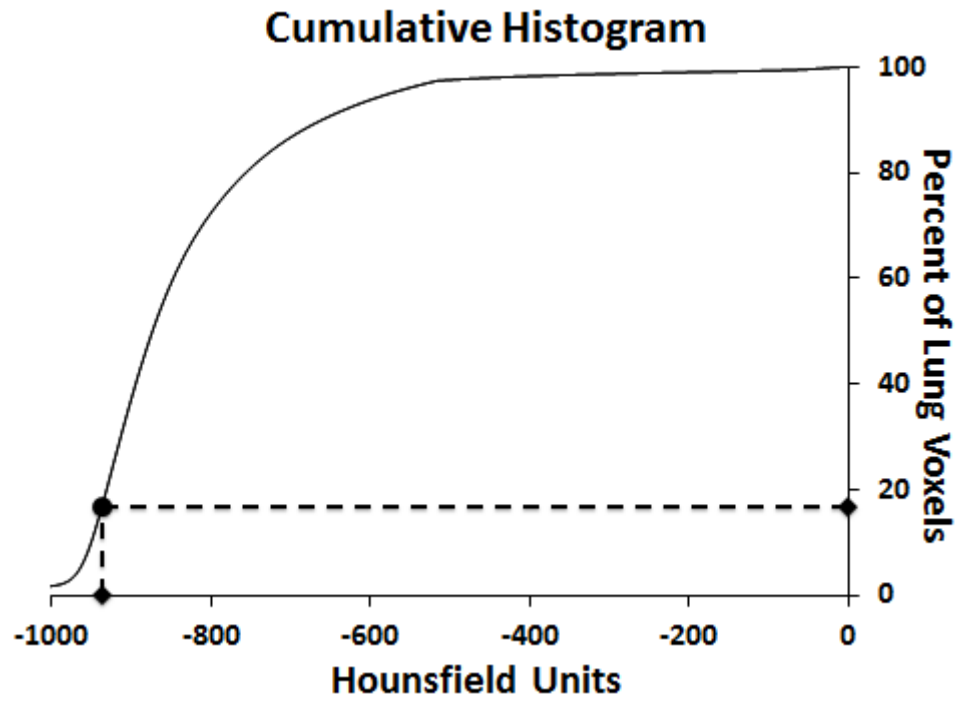
Figure 2. A cumulative histogram illustrating the threshold determining the amount of voxels below -950 HU, and hence the extent of emphasema-like region.
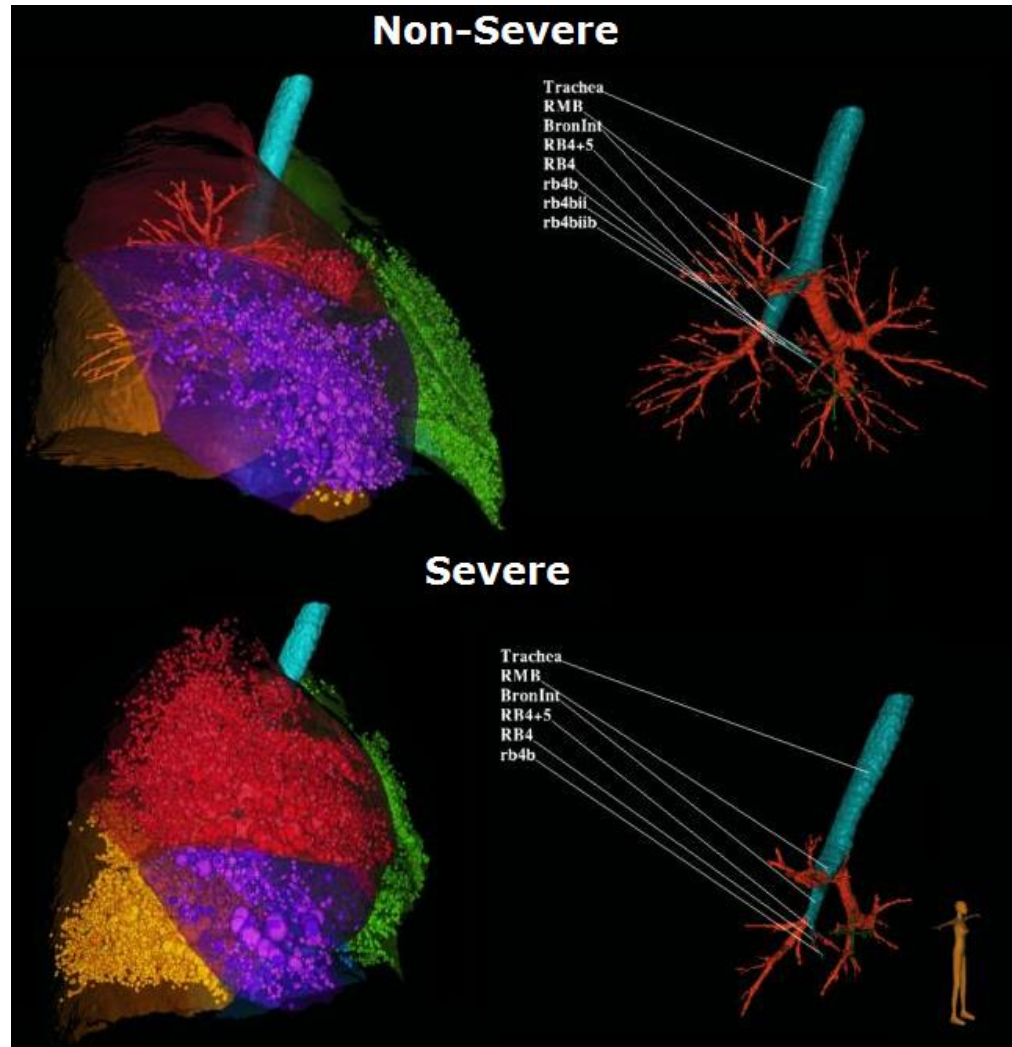
Figure 3. A volume-rendered image illustrating non-severe (*top set of lungs*) and severe (*bottom set of lungs*) air-trapping in an expiratory CT scan. Air-trappings are characterized in QCT by regions below -850 HU.

CHAPTER 2: CT TECHNOLOGY

Technology Advances

CT has emerged as a powerful method for imaging of the lung due to its high spatial resolution, high signal to noise ratio for lung tissue, fast acquisition speed, and widespread availability (18). Dual-source CT (DSCT) imaging can now provide anatomical, functional, and quantitative information about the lung with high temporal resolution. CT technology has quickly evolved from its introduction to medicine in the early 1970s (19), and its development through the decades has produced a profound change in the role of diagnostic imaging in medicine. A wide variety of medical conditions are visible in CT images that are not visible in traditional planar radiographs. Thus, diagnosis and monitoring of many diseases are possible through CT alone; this has reduced the amount of exploratory surgery previously required for these diseases. As a measuring device, the X-ray CT scanner has come a long way since its origins. Now, through standard calibration procedures, CT scanners measure so-called *CT numbers* in *Hounsfield units* (*HU*), which are meant to be constant from scan-to-scan and across different scanners, allowing for quantitative analysis in subjects.

CT is a reliable method for determining lung volumes and regional lung density. In order to quantitatively evaluate the lung, segmentation of the lung (20, 21), lobes (21, 22), airways (23-27) and vasculature (28, 29) are completed. Each voxel within the segmented regions of interest reflect the region density values which are based on X-ray attenuation.

CT numbers - the basis for QCT imaging - displayed in CT images show X-ray beam attenuation (μ) with respect to the attenuation of water, according to Hounsfield:

$$CT\ number = 1000\ (\mu - \mu_{water})\ /\ \mu_{water},$$

which defines the CT number of water as 0 HU, and air (with zero attenuation) as −1000 HU. On the positive range of the scale, there is no theoretical limit, however, medical scanners generally work in a range of −1024 HU to +3071 HU, with fat defined as -90 HU, blood 50 HU, muscle tissue 60 HU, and trabecular bone 300-500 HU.

During the early years of CT development, manufactures placed considerable effort towards lowering both the scanning and image reconstruction times. Accordingly, the time required to scan a patient and generate an image has dropped from several hours with the earliest clinical machines, to a small fraction of a second in modern machines. Multiple cross-sections can now be collected rapidly using both multislice and helical CT; hence, 3-D volume data sets are readily available.

Quantitative computed tomographic (QCT) imaging is increasingly used for phenotyping disease states of the lung. Chest CT measures have included mainly airway and parenchymal density based measures (7, 8). Many multicenter trials currently in progress focus on characterizing asthma (SARP), COPD (COPDgene), interstitial lung disease, or cancer lung screening programs all focus on phenotyping lung disease with these quantitative and structural measures. With all QCT imaging, reliable, repeatable, and accurate quantification of volumetric CT data for assessment of lung density, particularly for longitudinal and multi-center studies is necessary, yet, remains a challenge(30, 31).

Multi-Detector Row CT (MDCT)

Modern volumetric CT scanners move patients expeditiously through the X-ray beam field in order to acquire images with high temporal resolution, and to minimize

artifact from patient movement. As the imaging table moves in the z-axis (cranio-caudal or caudal-cranial) through the scan field, the X-ray tube and detector system perform multiple 360° rotations within the CT gantry to acquire a helical acquisition around the body. Mathematical algorithms, known as convolution kernels, are used to construct and then reconstruct image data. These algorithms use back-projection and iterative reconstruction techniques to interpolate dynamic sinographic data streams and produce a series of two-dimensional tessellated image slices. These two-dimensional image slices are then combined to create a three-dimensional volume, which can comprise of over one-hundred million volume elements, which are known as voxels.

MDCT scanners, which incorporate two-dimensional cone-beam projections, were introduced at the turn of the century (32, 33). MDCT imaging has greatly increases the z-axis coverage one X-ray tube rotation and has reduced scan times. In order to achieve this increased resolution and improve acquisition times, collimated cone-beam sources are used in conjunction with multiple rows of X-ray beam detectors and are used to acquire multiple image slices per-gantry rotation (34).

Most modern medical CT scanners use just one X-ray source due to the initial cost and maintenance costs associated with X-ray tubes. However, in more recent years, dual-energy (DE) and dual-source dual-energy (DSDE) CT scanners have been produced to exceed the limits of single-source single energy (SS) CT scanners.

<u>Dose & Noise</u>

The fundamental radiation dose parameter in CT is the computed tomography dose index (CTDI) (35). CTDI is a measured value that uses distinctive thermoluminescent (often LiF) dosimeters that need to be manually analyzed in order to

determine the dose incurred for a given scan (36), it is therefore not widely used. $CTDI_{100}$ is a more expedient measure for the clinical setting and is obtained through the use of an ionization chamber that is placed within the scan field of view prior to patient imaging, the ionization chamber is a gas-filled radiation detector that creates a measurable charge which is counted over the length of a single 100 mm axial to determine radiation exposure under a variety of scanning energies and tube currents (37, 38). The $CTDI_{100}$ measure assumes a homogenous dose distribution through a body, however, it is known that the periphery of an object (e.g. skin) absorbs a relatively higher amount of dose, compared with the center of the body. The $CTDI_w$ measure was created to account for this, and is based on simple weighted averages from $CTDI_{100}$ measures taken from central and peripheral regions on ionization chambers. For each, the $CTDI_{100}$ and $CTDI_w$, the measures of exposure are converted to an estimated dose for an idealized 70 kg, 30-year-old patient (39, 40). With the advancement in volumetric CT imaging, a more recent derivation of the $CTDI_w$ is the volume CTDI ($CTDI_{vol}$), which is the radiation dose parameter that has been specified by the International Electrotechnical Commission to ensure consistency in dose reporting across manufacturers (41). The main advantage of $CTDI_{vol}$ over $CTDI_w$ being that $CTDI_{vol}$ averages radiation dose in a volume (i.e. x, y, and z directions), and not just a single slice (i.e. x-y plane). The equation for $CTDI_{vol}$ is defined as:

$$CTDI_{vol} = \frac{n*T}{l} * CTDI_w = \frac{1}{pitch} * CTDI_w$$

where l is the slice spacing (in mm), T is the nominal slice thickness (in mm), and n is the number of slices. The conventional unit for radiation dose is the rad., however,

measured CTDI results are typically reported in SI units as the gray (Gy), which and are representative of absorbed dose (42).

Dose is related to noise in an image by Poisson distribution, i.e. quantum (beam), and is congruent with the signal to noise ratio (SNR) in an image (43). In addition to the influence of dose in image quality, a number of other factors play important roles in overall image quality. As evident by the CTDI$_{vol}$ equation, dose is related to pitch which is related to slice thickness, and pixel dimension (image resolution) (Δ) such that we can expand our equations to:

$$Dose \propto \frac{SNR^2}{\Delta^3 T}$$

for example, if one attempts to reduce the pixel size (increasing the image spatial resolution) and maintains the same effective dose, the image with higher spatial resolution would see fewer X-ray photons passing through it, and therefore the SNR per pixel would drop.

<u>Quantative CT Principles</u>

X-ray works on the principle of the Beer-Lambert Law, which states that there is a logarithmic dependence between the transmission of a wave (i.e. X-ray photon beam) through a substance, the product of the attenuation coefficient of the substance, and the distance the wave travels through the material (i.e. path length). This law can be derived to take the form:

$$I = I_0 \, exp(-\mu x),$$

where I is the transmitted beam intensity, I_0 is the measured beam intensity, μ is the linear attenuation coefficient, and x is the material thickness. Beam transmission (I/I_0) through a given object varies with beam energy, and accounts for measurable changes in

attenuation coefficients, which directly correlates to CT numbers using a previously described Hounsfield equation. This is particularly pronounced in projections through heavier elements. Regions of interest (ROIs) can be enhanced by contrast elements containing high atomic numbers, such as iodine (Z=53) and xenon (Z=54), which can be readily differentiated from calcium (Z=20) and other anatomical structures, including fat and tissues (44).

Not all of a diagnostic X-ray photon beam is simply absorbed or allowed to pass in a straight line through an object. Beam attenuation is the result of both the absorption and the scattering of photons due to interactions with the atoms and electrons that are between the X-ray source and detector. Scatter is the result of a radiation beam changing its expected path as it passes from an X-ray tube to detector, and is one of the leading causes of diagnostic projection degradation, and along with beam hardening, is one of the major known causes of CT image artifacts (45), with HU deviation from expected CT values as high as 300 HU seen in early generation cone-beam CT (46).

As photons pass through an object, one of three primary types of scatter interactions can occur: Compton scatter, photoelectric absorption, and coherent scatter. The individual contributions of these phenomena are dependent on the energy of the X-ray spectra being used, and on the material properties of an object under analysis (47).

The least significant of these three forms of scatter is coherent (also known as Thomson or Rayleigh scatter). With coherent scatter, the full energy of the photon is absorbed by the electrons of an atom, and subsequently re-emitted with its original energy, in a random direction.

With photoelectric absorption, the full energy of the photon is absorbed, which results in the ejection of an electron from the outer shell of the atom, causing ionization of the atom. As the ionized atom returns to its neutral state, a low energy X-ray photon is emitted from the atom, however, this low energy photon is typically absorbed by other materials or filters and is not a significant source of scatter related noise in modern CT scanners.

Compton scattering is the result of an inelastic deflection of an X-ray photon from its original path by an interaction with an electron. The result is a decrease in energy (increased wavelength) for the incident photon, which is proportional to the angle of deflection. Total energy and momentum of the system is conserved as the lost photon energy is used to eject an electron, ionizing the atom. Compton scattering is named after the physicist who first observed the phenomenon and derived a relationship between scatter angle and change in wavelength in 1923, Arthur Compton. This relationship is expressed as:

$$\lambda' - \lambda = \frac{h}{m_e c}(1 - cos\theta),$$

where λ is the initial wavelength, λ' is the wavelength after scattering, h is Planck's constant, m_e is the mass of the electron at rest, c is the speed of light, and θ is the angle of scatter. Unlike the other forms of scatter, Compton scattering has a significant impact on qualitative and quantitative CT imaging, due to CT detectors being unable to differentiate between these scattered X-ray photons. As an illustration of this, if a 100 keV photon (λ = 0.0124 nm) is deflected 90 degrees (a relatively extreme deflection angle), only 16 keV of kinetic energy would be transferred to the ejected electron, and the resultant 84 keV X-ray photon (λ' = 0.0148 nm) would still be within a filtering window

of energy detection on a clinical CT system. At a between 5 degree scattering angle, the incident photon energy is nearly unchanged.

<div align="center">Two-Material Decomposition</div>

Contrast in CT is based on the X-ray photon attenuation characteristics of different materials, and is associated with the tissue densities and specific composition of elements in the material. For a non-contrast enhanced, single energy, lung volume scan, if we consider the that the lung is composed of two materials -- e.g. "tissue" (including blood) at 50 HU and air at -1000 HU – then, using the conservation of mass, the fraction of HU density related to "tissue" and air within a volume can be can be calculated for each voxel in a region of interest (**Fig. 4**) (48). In simplified formula, the equation for this is:

$$F_{air}CT_{air} + F_{tissue}CT_{tissue} = CT$$

$$F_{air} + F_{tissue} = 1$$

where F_{air} and F_{tissue} are the voxel fraction of air and tissue. CT is CT numbers in HU at a given energy level. CT_{tissue} may be considered as 50 HU and CT_{air} is -1000 HU (49, 50). For example, to determine the percent tissue in a given voxel the equation can be derived as:

$$F_{air} = \frac{CT - CT_{air}}{CT_{tissue} - CT_{air}}$$

Total lung volumes are determined by the summation of segmented voxels in each slice, multiplied by conversion factors, based on slice thickness and image field of view, to produce perceptible results. By combining the total lung volume with tissue or air fractions, the absolute volumes of these materials in the lung are determined (48, 51, 52).

Dual-Energy CT Principles

In any single projection measurement, we can only isolate two materials, e.g. water and air. However, using two energy beams, and exploiting known attenuation properties, a three-material decomposition can be performed. This allows us to effectively perform two scans in one and isolate contrast materials, with one radiation exposure and near perfect slice overlap, which is beneficial in the clinical environment where patient movement and radiation dose are a concern. In essence, dual-energy imaging works by imaging the same space in a single exposure, at two separate energies, e.g. one at 80 or 100 kVp and the other at 140 kVp, and deriving two separate attenuation measures to better understand the composition of an object.

Three-Material Decomposition

Analogous to two-material decomposition, three-material decomposition can be performed using the conservation of mass assumption, i.e. the sum of the three mass fractions is equivalent to the mass of the whole mixture (1, 53).

Using this assumption, we can construct three simplified fundamental equations similar to (53), (54) and our two material decomposition equation:

$$F_{air}CT_{air,E1} + F_{tissue}CT_{tissue,E1} + F_{contrast}CT_{contrast,E1} = CT_{E1},$$

$$F_{air}CT_{air,E2} + F_{tissue}CT_{tissue,E2} + F_{contrast}CT_{contrast,E2} = CT_{E2},$$

$$F_{air} + F_{tissue} + F_{contrast} = 1,$$

where $E1$ and $E2$ represents values acquired from scans at different energies, e.g. 80 kVp and 140 kVp. And *contrast* is typically iodine due to its stronger enhancement at low tube voltage settings, in addition to its physiologic properties (55).

Using these three equations, we can therefore derive the following matrix to determine the fractional content of the materials inside a voxel or object:

$$
\begin{bmatrix} F_{air} \\ F_{tissue} \\ F_{contrast} \end{bmatrix} = \begin{bmatrix} CT_{air,E1} & CT_{tissue,E1} & CT_{contrast,E1} \\ CT_{air,E2} & CT_{tissue,E2} & CT_{contrast,E2} \\ 1 & 1 & 1 \end{bmatrix}^{-1} \begin{bmatrix} CT_{E1} \\ CT_{E2} \\ 1 \end{bmatrix},
$$

in practice, this allows for an isolation of contrast material in a volume. In addition to the isolation of contrast medium, by taking the weighted sum of images acquired at separate energies, and subtracting the image containing just the contrast enhancement, you effectively produces both a perfectly registered contrast enhanced image, and a "virtual non-contrast" (VNC) image derived from a single exposure (47).

Although the three-materials mentioned herein were for *air*, *tissue*, and *contrast*, any three materials can feasibly be isolated. For example, in liver parenchyma we can isolate fat, soft tissue, and iodine. By deducing that the stronger image enhancement at 80 kVp in relation to that of 140 kVp in an 80 kVp / 140 kVp DSDE scan is attributed to a certain concentration of iodine, we can perform a weighted and smoothed image subtraction to map the iodine content within the image (47). This same methodology can be used to easily remove any contrast material in image space, and can also be used to remove bone, as calcium has a relatively high Z. It is theoretically possible to discriminate between types of body tissue (e.g. vascular, scar, cancerous and muscle tissues) without the use of a contrast agent, however, since these tissues have a similar composition of basic biological atoms (carbon, hydrogen, oxygen, and nitrogen) which each demonstrate very similar X-ray attenuation characteristics at different energies due to their similar atomic numbers (Z ranges from 1-8), any differentiation of soft tissues without the use of contrast has proved to be a challenge (2, 56).

Dual-Source Scatter Correction Methods

Dual-energy CT (DECT) scanners operate in a pulse mode which excites a single X-ray tube at alternating kVps (80 and 140 kVp, for example) in staccato. This switching of kVp within a single scan provides great technical challenges with rapid gantry rotation and can lead to certain functional limitations in imaging protocols, due to such factors as tube overheating (57, 58). As an alternative, dual-source CT (DSCT) systems utilize two measurement systems on the same slip ring, A and B, offset by approximately 90° (**Fig. 5**).

The first generation of clinical DSCT scanners was introduced in 2006 (59, 60), while the second generation (Definition Flash, Siemens Healthcare, Forchheim, Germany) became available in 2009 (61). The Definition Flash scanner used in this work has two X-ray tube/detector systems (A and B) positioned on the gantry with 95° angular off-set from each other. Tube A in the Definition Flash has a standard scan field of view (FOV) of 50 cm, while tube B has a smaller FOV of 33 cm. In a single-source (SS) mode, the scanner only uses tube A and its operation is essentially identical to that of conventional single-source CT. In a dual-source (DS) mode, the scanner can operate with both tubes running at the same kVp as in cardiac or high-pitch modes when projection data from both tubes are combined in a single image dataset. It can also operate in a dual-source dual-energy (DSDE) mode when both tubes run independently at different kVp (high and low energy) and projection data from each tube are reconstructed to produce two independent image datasets. These datasets can be further used for dual energy post-processing (1) or combined (e.g., by linear mixing (62)) to generate a single dataset similar to conventional single-source CT. To improve the separation between the

high and low-energy spectra in the DSDE mode, and to further harden the multispectral beam, tube B is equipped with an additional beam-hardening tin filter (63).

When operating in a DS mode, scattered photons from tube A can impact on detector B and vice versa representing "cross-scattered" radiation (**Fig. 6**) which needs to be taken into account and compensated (64, 65). Without adequate scatter correction, scatter has been known to degrade image quality and produce artifacts by reducing the contrast-to-noise ratio (CNR) in an image (66). Correction algorithms are necessary to diminish the negative effects of scattered radiation (67). To deal with this problem, DSCT scanners employ dedicated cross-scatter correction techniques which were further improved for the second-generation DSCT, and has the added benefit of compensating for "forward-scatter" radiation, which occurs when a photon from tube A impacts detector A after being deflected from its expected straight-line path (**Fig. 6**) (68).

Both detector modules of a Definition Flash scanner are equipped with dedicated sensors located outside the cone beam in the z direction, which are used for an on-line measurement of both cross-scattered and forward-scattered radiation during a DSCT scan. In a SS mode (as in conventional CT), forward-scattered radiation is expected to be blocked by an anti-scatter grid of the detector module and, hence, a dedicated forward-scatter correction is not employed.

This scatter correction technique forms the basis for the correction algorithms used in, and only in, the dual-source mode of the Siemens Definition Flash 128 scanner which are used in our experiments.
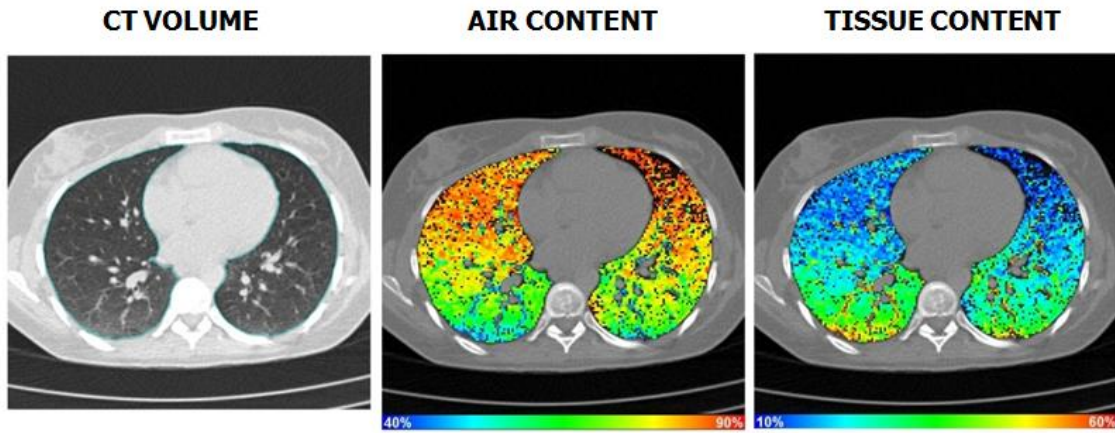
Figure 4. An illustrated color-mapping the air (*center panel*) and tissue (*right panel*) content using a two-material decomposition on a chest CT dataset.
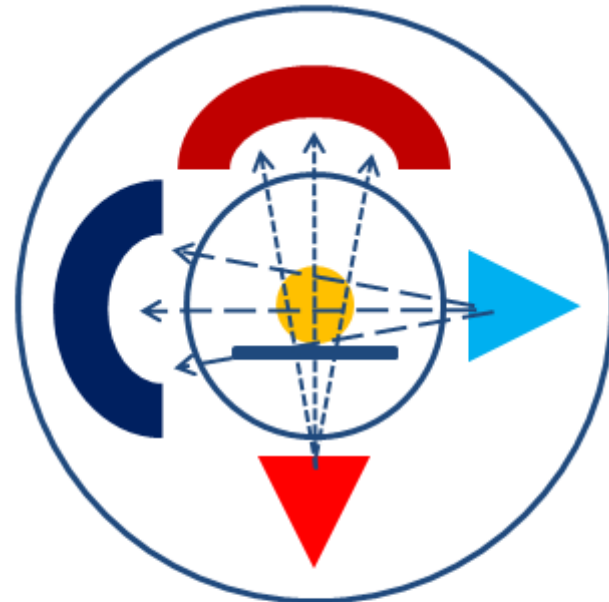
Figure 5. An image illustrating the configuration of a dual-source CT (DSCT) gantry.
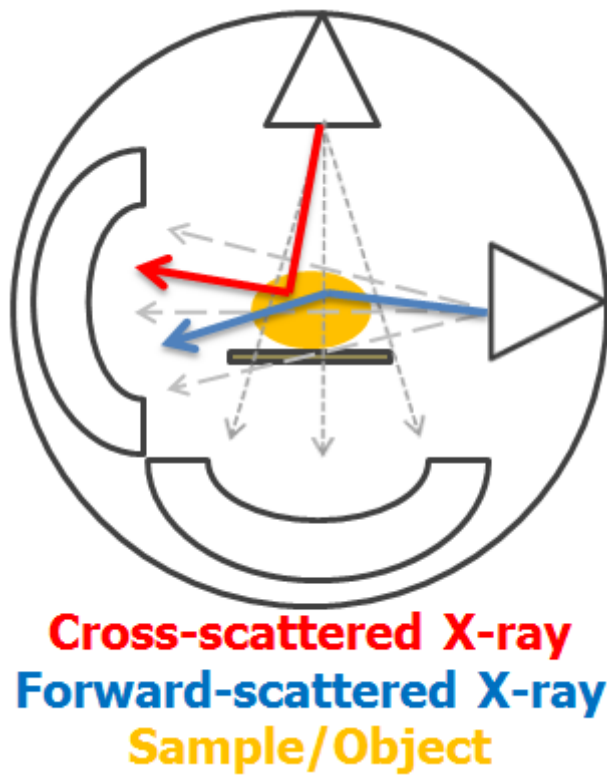
Figure 6. An illustration of cross-scatter (*red*) and forward-scatter (*blue*) radiation in dual-source CT (DSCT) imaging.

CHAPTER 3: QUANTITATIVE ASSESSMENT OF LUNG MEASURES IN DUAL-SOURCE COMPUTED TOMOGRAPHY

Introduction

Quantitative computed tomographic (QCT) imaging is increasingly used for the characterization of the lung (69-74), yet, reliable, repeatable, and accurate quantification of volumetric computed tomography (CT) data for assessment of lung density, particularly for longitudinal and multi-center studies remains a challenge. It has been observed that air in the trachea of a chest CT scan is often significantly different from its true value of -1000 Hounsfield Units (HU), and this varies between scanner makes and models (30, 75). The variability of intra-thoracic air HU measurements across sites, scanner makes and models limits the accuracy when measuring air trappings and the extent of emphysema-like lung parenchyma, which has been defined as the percentage of voxels below -950 HU within the lung field on volumetric CT scans (76-89) or the HU value below which 15% of lung voxels fall (P15) (90). The variability in intrathoracic air values makes comparisons between CT scanner makes and models challenging.

The motivation for this study was our preliminary observations in animal experiments that air in the trachea was consistently closer to -1000 HU when using Siemen's Somatom Definition Flash dual source dual energy (DSDE) scan mode compared to the same scanner's single source (SS) scan mode. The primary difference between the DSDE and SS modes is the implementation of a dedicated hardware-based scatter correction in the DSDE mode while the SS mode simply uses an anti-scatter grid which is expected to block all scattered radiation. Therefore, the goal of this study was to

test the hypothesis that the scatter-correction employed in the DSDE mode results in more accurate (closer to the nominal -1000 HU) CT numbers of air in the trachea compared to the anti-scatter grid solution typical for conventional single-source CT.

Materials and Methods

The Siemens Somatom Definition Flash (Siemens Healthcare, Forchheim, Germany) scanner (61) used in this study has two x-ray tube/detector systems (A and B) positioned on the gantry with 95° angular off-set from each other. Tube A has a standard scan field of view (SFOV) of 50 cm, while tube B has a smaller SFOV of 33 cm. In a single-source (SS) mode, the scanner only uses tube A and its operation is essentially identical to that of conventional single-source CT. In a dual-source (DS) mode, the scanner can operate with both tubes running at the same kVp as in cardiac or high-pitch modes when projection data from both tubes are combined in a single image dataset. It can also operate in a DSDE mode when both tubes run independently at different kVp (high and low energy) and projection data from each tube are reconstructed to produce two independent image datasets. These datasets can be further used for dual energy post-processing(1) or combined (e.g., by linear mixing(62)) to generate a single dataset similar to conventional single-source CT. To improve the separation between the high and low-energy spectra in the DSDE mode, tube B is equipped with additional tin filter(63). The DSDE mode can be operated using only 3 different A/B kVp combinations (80/140Sn, 100/140Sn and 140/80, where Sn stands for the tin filter)

The scatter-correction technique for the dual-source scanner in DSDE mode relies on a direct measurement of the scatter amplitudes with scatter sensors close to the detector, but outside the penumbra of the fan beam. Measurement based scatter correction

addresses both cross-scatter and forward scatter and it uses the actual scatter profiles instead of approximate model-based profiles. Therefore, it shows an improved performance over model-based scatter correction and it is applicable to larger patients and wider detectors(67). The scanner does not take advantage of this measurement-based correction in the SS mode.

Study Outline. Using both phantom and animal models (described below), we compared the quantitative results of scans acquired using the SS and DSDE modes. Image data from tube A could be compared between the SS and DSDE modes at 80, 100 and 140 kVp.

In the phantom model, we independently controlled the current of each x-ray tube in the DSDE mode. This allowed us to practically eliminate the effect of cross-scatter by setting the current of one tube to its minimum (near zero) value while using the data from the other tube. Thus, the scatter contribution was dominated by forward-scattered radiation; very similar to conventional single-source CT. Throughout the remainder of this paper we refer to this mode as "DSDE-SS." We would like to emphasize that the DSDE-SS mode is just a partial realization of the DSDE mode and, hence, both the DSDE and DSDE-SS modes use exactly the same scatter correction technique based on real-time measurements of scattered radiation. The only difference between them is the additional contribution of cross-scattered radiation in the DSDE mode, which can be neglected in the DSDE-SS mode. On the contrary, the SS mode does not employ a dedicated scatter correction and uses a simple anti-scatter grid solution to block forward-scattered radiation.

The images acquired in the SS mode were reconstructed with the B35f kernel that is traditionally used for quantitative CT applications such as coronary calcium scoring. The images acquired in the DSDE and DSDE-SS modes were reconstructed using both B35f and the dedicated D30f kernel designed for the use with dual-energy post-processing, which is highly dependent on accurate CT numbers. The B35f and D30f kernels have similar (medium strength) sharpness and no edge enhancement. The edge enhancement feature can modify CT numbers in the edge vicinity and, hence, affect the accuracy of CT numbers.

Animal Models

The Institutional Animal Care and Use Committee approved all animal studies reported here. Six farm-bred ovine (39.2 ± 1.8 kg; 4 female) and 13 farm-bred swine (33.4 ± 3.1 kg; 8 females) were premedicated with Ketamine (20 mg/kg) and Xylazine (2 mg/kg) intramuscularly, and anesthetized with 3–5% isoflurane in oxygen by nose cone inhalation. Once surgical depth of anesthesia was achieved, an 8.0-mm inner diameter cuffed endotracheal tube was placed through a tracheostomy and the animals were mechanically ventilated with 100% oxygen, tidal volume of 10-14 mL/kg, rate of 10-20 breaths/min adjusted to achieve an end-tidal PCO_2 of 30–40 mm Hg. Carotid arterial and external jugular venous introducers were placed. Surgical plane of anesthesia was maintained with inhaled isoflurane (1–5% in oxygen), neuromuscular blockade was achieved with pancuronium (0.1 mg/kg IV initial dose and 0.5–1 mg/kg hourly as needed). Arterial pressure, oxygen saturation, and airway pressures were continuously monitored and recorded. Animals were placed supine on the scanner table and were held with gentle forelimb traction. Consistent static breath-holds were achieved through the

use of an adjustable water column positioned next to the scanner, to provide 20 cmH2O airway pressure during the breath-hold with a flow through of 3-5 L/min of room air to maintain backpressure, connected to the proximal end of the endotracheal tube.

Swine and ovine were included to determine if thorax shape had an effect on the quantitative measurements in our scans. As seen in the top row of **Figure 7**, ovine have a more conical and deep dorsal to ventral dimensioned thorax, while swine have a more ovoid and human-like thorax.

Animals were scanned in the SS mode (80, 100, 140 kVp), and in the DSDE mode (80/140Sn kVp, 140/80 kVp, and 100/140Sn kVp) while exploring the effect, if any, of varying available scanning parameters. Such parameters included rotation time (0.28, 0.33, or 0.5s); pitch (0.45, 0.55, or 1.0); slice thickness (0.6 or 0.75mm); scan direction (cranio-caudal or caudo-cranial); detector collimation (64 or 128); and reconstruction kernel (B35f or D30f). A consistent CTDIvol of 12 (+/- 0.1)mGy was used for all scans, except the dose controlled scans which had a CTDIvol of 6 (+/- 0.1)mGy.

Analysis. Semi-automated airway and whole lung segmentations of the animal scans were performed using the Pulmonary Analysis Software Suite (PASS) (49). To ensure that only lung tissue or tracheal air was used in voxel densitometry calculations, resultant segmentations from PASS were spherically eroded by 3 voxels in the trachea, and 10 voxels in the whole lung to minimize contamination by the chest wall, mediastinum or tracheal wall. Airway segmentation was then limited to only include the tracheal lumen between the end of the distal endotracheal tube and the carina. To avoid the early right bronchus take-off in these animals, the endotracheal tube was situated just distal to the vocal folds. Additional manual segmentations were taken of the inferior

vena cava (IVC) between the diaphragm and the base of the heart, being careful to avoid any partial volume effect from the lung and keeping distance from the heart to avoid any motion artifact. The tracheal, IVC, and lung parenchymal regions of interest (ROIs) were compared for each of two scanning modes (SS & DSDE). Unlike the phantom studies, in the animal studies we did not do the DSDE-SS because this mode was not available at the time of scanning.

<center>Phantom Protocol</center>

We used a variant of the COPDGene Phantom (91) (Phantom Laboratories, Salem, NY) (**Fig. 8,** *upper panel*). This phantom consists of an outer ring that has the x-ray attenuation characteristics similar to water (7-20 HU). The inside of the ring contains a foam material (sampled in region **B of Fig. 8**) with an average CT attenuation close to that of lung parenchyma (~-860 HU). There are three inserts within the foam material in the phantom: a 3.2 cm polymer bottle filled with distilled water (**E in Fig. 8**), a 3 cm air hole (**C in Fig. 8**) and a 3 cm acrylic rod (**D in Fig. 8**). In addition to the air within region C, a second air region (**A in Fig. 8**) is surrounded by an acrylic ring simulating attenuation of the mediastinum and tracheal wall to better represent potential tracheal air artifacts.

The phantom was scanned in the SS mode (80, 100, 120 and 140 kVp), in the DSDE mode (80/140Sn kVp, 140/80 kVp, and 100/140Sn kVp), and in the DSDE-SS mode (the same combinations as in the DSDE mode but with tube A or B set at min mAs). A consistent CTDIvol of 12 (+/- 0.1)mGy was used for all scans, except the dose controlled scans which had a CTDIvol of 6 (+/- 0.1)mGy. Additional controlled scans were acquired comparing: rotation time (0.33 or 0.5s); pitch (0.55 or 1.0s); slice thickness

(0.6 or 0.75mm); slice spacing (0.5 or 0.6mm); scan direction (cranio-caudal or caudo-cranial); number of detectors used (64 or 128); and reconstruction kernel (B35f or D30f).

Analysis. The phantom inserts were manually segmented across the central third of the z-axis extent for each of the five distinct regions of interest (actual ROIs are approximated by the illustrative dashed lines: A, B, C, D, E shown in the upper panel of **Fig. 8**), being careful to avoid any partial volume effect from the wall regions. The same ROI placements were used for each scan (SS, DSDE or DSDE-SS) acquired in the phantom experiment. Voxel densitometry measures of mean, median, mode, and standard deviation were then recorded along with histogram results.

Two-tailed paired difference t-tests were performed on both phantom and animal models by taking the mean density values within segmented regions of a SS scan and comparing it to the corresponding region on a DSDE or DSDE-SS scan. A Bland-Altman plot of the mean of SS & DSDE vs. the difference between them was constructed for both the phantom and animal models in the lung parenchyma and trachea regions. These plots were constructed using the mean difference on a slice-by-slice basis in both 80 and 140 kVp scans along the transverse axis of the segmented region of interest. An axial profile plot was constructed to show the relationship between the mean lung densities and the difference within individual transverse lung section along the z-axis.

Results

Animal Study

The animal study demonstrated that, within the lung and tracheal regions of both ovine and swine, the mean and median of the density histograms are close to -1000 HU when running the scanner in the DSDE mode (**Fig. 7**), while the mean and median are

shifted significantly ($p < 0.001$) towards more positive HU values (representing increased attenuation) by 32HU on average when using the scanner in the SS mode (**Table 1**). This behavior (shown in **Fig. 7,** *middle and lower panels* for 140 kVp) was observed for all three kVp values of tube A (80, 100 and 140) used in the DSDE vs. SS comparison. There is a statistically significant ($p < 0.001$) quantitative shift in CT numbers seen in the IVC when comparing SS and DSDE modes. Unlike in the less dense, more air-like, regions of thorax – where DSDE mode measures are more negative – the HU shifting within the more dense (relative to lung parenchyma) IVC blood is in the positive direction (**Table 1**).

In the DSDE mode, the normalized density histograms derived from the images reconstructed with the B35f and D30f kernels were nearly identical. This is expected. As discussed above, the physical characteristics of both kernels are similar. No other acquisition/reconstruction parameters showed an effect on the mean and median values of the density histograms.

A plot of the SS vs. DSDE air values sampled from a representative ovine trachea (**Fig. 9,** *top, left-panel*) demonstrates a relatively uniform attenuation throughout the trachea in the DSDE scans with considerable variability in air values sampled from the SS scans. A Bland-Altman plot from the same ovine trachea (**Fig. 9,** *top, right-panel*) demonstrates a mean biased slope of 1.84, with the mean difference being 18.70HU between the SS and DSDE scan. The lung parenchyma (**Fig. 9,** *bottom, left-panel*) shows a good correlation between the SS and DSDE scans. However, the Bland-Altman plot (**Fig. 9**, *bottom, right-panel*) shows a bias in the opposite direction to the trachea with a slope of -0.0871 and a mean difference of 6.25HU. The Bland-Altman plot could be seen

as a series of upward sloping relationships that mimic the tracheal relationship, possibly representing varying slice-to-slice dominance of larger vs. smaller bronchial segments. While details are slightly different between ovine and swine data sets, all animals showed similar relationships as demonstrated in **Figure 9**. To demonstrate the local effects of thoracic structures on scatter, in **Figure 10** we provide plots of lung density vs. base-to-apex distance along the lung plotted against the difference between the DSDE and SS scans. The mean lung density represents the mean of the DSDE and SS slice means. Difference plots (**Fig. 10**, *left-panels*) demonstrate the relationship between the mean slice density and the difference in the HU values between SS and DSDE scans along the z-axis of a swine and an ovine respectively. The relationship between structure shown as anterior-posterior and lateral volume renderings and scatter correction effects are highlighted by the shaded areas color coded similarly in the right and left panels. Note that the DSDE vs. SS differences are greatest in the apical regions of the thorax where scapular, sternal and spinal structures converge to cause the greatest amount of scatter, accounted for by the scatter corrections inherent to the DSDE imaging.

Phantom Study

Similar to the animal experiment, a statistically significant (~16HU, $p < 0.001$) shift between the mean HU values derived from the SS and DSDE modes (**Fig. 8**) was observed in the "tracheal" region of the phantom (**Fig. 8**, *region A*), with the DSDE scans producing CT numbers closer to the nominal air value of -1000HU. This shift was essentially the same when using either the DSDE or DSDE-SS modes (which showed a correlation of $p < 0.05$ with each other) and was similar for all kVp values.

The phantom inserts representing different materials demonstrated the HU shifts of varying magnitudes, directions and significances (**Table 2**). For example, in the region simulating the trachea, the difference is significant at over 15HU, with the DSDE scan resulting in a more negative HU value. Meanwhile, in the acrylic region, the difference between the two scan modes was over 20HU when comparing 140 kVp values, with the DSDE scan resulting in a more positive HU value.

The observed DSDE vs. SS behavior remained similar across all acquisition/reconstruction parameters used in the experiment, though some of the parameter changes were blunted (**Table 3**). Standard deviation (image noise) in the DSDE mode was consistently higher than in the SS or DSDE-SS modes. This is expected because matching $CTDI_{vol}$ between the DSDE and SS modes resulted in much lower dose per tube for the DSDE mode because the $CTDI_{vol}$ is split between the two tubes.

Plots obtained from the phantom (**Fig. 11**) are shown in formats similar to the in vivo plots represented in **Figure 9**. While the trends between the phantom and animal studies are similar, the phantom is missing the sloping relationship seen in the Bland-Altman plots because of the missing added scatter effects associated with anatomic structure. Bland-Altman plots in the phantom "trachea" segment (**Fig. 11**, *top, right-panel*) show a steady difference of mean slice values, with the mean difference being 13.89HU between the SS and DS scan. Similarly, the "lung" segment (**Fig. 11**, *bottom, righ- panel*) shows a consistent difference of 3.85 HU.

Discussion

Our animal and phantom studies demonstrated that the Definition Flash scanner provided more accurate CT numbers of air within the in-vivo trachea and within the

trachea-like portion of the phantom when the scanner was operated in the DSDE mode. A significant positive shift of 15-35 HU in the animal and phantom experiments was consistently observed when the scanner was operated in the SS mode representing scanning similar to that used in a conventional single-source CT. An overall smaller (but significant) shift on the order of 10 HU was observed for the whole-lung histograms; these shifts are markedly more apparent in anatomically dense, and complex regions, e.g. the apical lung regions.

Even though there are many different confounding factors that potentially shift CT-derived air values from the nominal value of -1000 HU, the two most likely causes are scatter and beam hardening. To the best of our knowledge, the beam hardening correction is the same for both SS and DSDE modes of operation. On the other hand, the anti-scatter solutions are very different between the two modes. The SS mode relies on the grid of anti-scatter collimators located at the detector level to block all scattered radiation and, hence, no specific scatter correction method is used. On the contrary, the DSDE mode relies on the correction method based on real-time measurements of scattered radiation. Therefore, the results of this study suggest that the dedicated scatter correction technique employed by the Definition Flash. (67) in the DSDE mode plays a major role in generating more accurate CT numbers for tracheal air which are closer to the nominal value of -1000 HU.

Dual-source CT (DSCT) requires a very different approach for scatter correction compared to conventional single-source CT. With both tubes operating simultaneously, scattered photons originating from tube A can be detected not only by detector A (i.e., forward scatter as in conventional CT) but also by detector B and vice versa resulting in

cross-scattered radiation. Compensation for cross- scattered radiation were reported for the first generation DSCT (92) and modified for the second generation DSCT (67). The later scatter correction method employs on-line measurements of both cross-scattered and forward-scattered radiation during a DSCT scan. When the full beam collimation (128x0.6 mm) is used, these measurements are done using the dedicated sensors located outside the cone beam in the z direction. When a partial beam collimation (e.g., 64x0.6 mm) is used, these measurements are done using the outer detector rows outside of the collimated beam.

More accurate CT numbers of air produced by the DSDE mode can be attributed to a better compensation of forward-scattered radiation by use of added scattered radiation sensors, placed on both sides of the primary detector module compared to the SS mode that only relies on the anti-scatter collimators placed above the primary detector pixel elements (67). These added scatter radiation sensors in DSDE mode result in additional compensation for forward-scattered radiation which is not completely blocked by the anti-scatter collimators. (67). The phantom scans done in the DSDE-SS mode provide evidence in support of this statement because both the SS and DSDE-SS modes were predominantly affected by forward-scattered radiation.. Moreover, no difference between the phantom results obtained in the DSDE and DSDE-SS modes indicates that the cross-scatter contribution is properly compensated and does not have a detrimental effect on the accuracy of air CT numbers.

Improving the accuracy of air CT numbers in the trachea and the lung parenchyma is of great importance for quantitative CT (QCT) lung imaging. Since all QCT lung measures (e.g., percentage of emphysema and air trapping) are based on the

absolute HU thresholds (e.g., -950 HU for emphysema), shifts in air CT numbers on the order of 20-35 HU (as observed in this study) can result in significantly shifted estimates of percent emphysema scores. This is especially important for longitudinal and multi-center studies that involve scanners of different makes and models as well as scanner changes between time points. Because our results suggest that scatter correction serves to correct air values within both the in vivo lung scans as well as the phantom (more so in the in vivo scans) we conjecture that non-ideal compensation of forward-scattered radiation is likely a major factor responsible for the deviation of air CT numbers from the nominal value of -1000 HU. Therefore, we believe that lung QCT can benefit from forward-scatter correction (93-95). Furthermore, the upward sloping tracheal Bland-Altman plots (**Fig. 9**, *top*) along with the variable scatter effects on apical lung parenchyma (**Fig. 11**, *top* and *bottom*) suggest that efforts to retrospectively correct lung attenuation based upon tracheal samples may be ill-advised.

In this study we only focused on the effect of scatter correction and did not investigate the effect of beam hardening which, for example, is well known to cause significant changes in CT numbers of iodine (96). Such investigation would involve scanning phantoms in a wide size range, while the phantom we used in this study was available only in one size. Nevertheless, no significant difference in the air CT numbers obtained at different tube energies ranging from 80 to 140 kVp (except a small ~3-6HU shift at 140Sn kVp) suggest that beam hardening is probably of less importance compared to scatter, at least under conditions of our experiments. Furthermore, because the same beam hardening correction algorithm is used in both DS and SS modes, we felt

that the data presented provides the strongest evidence for scatter being the likely source of air value offset in the SS scanning mode.

In conclusion, our study suggests that the dedicated scatter correction technique employed by the DSDE mode of a second generation DSCT scanner results in more accurate CT numbers of the tracheal air compared to the SS mode representing conventional single-source CT.
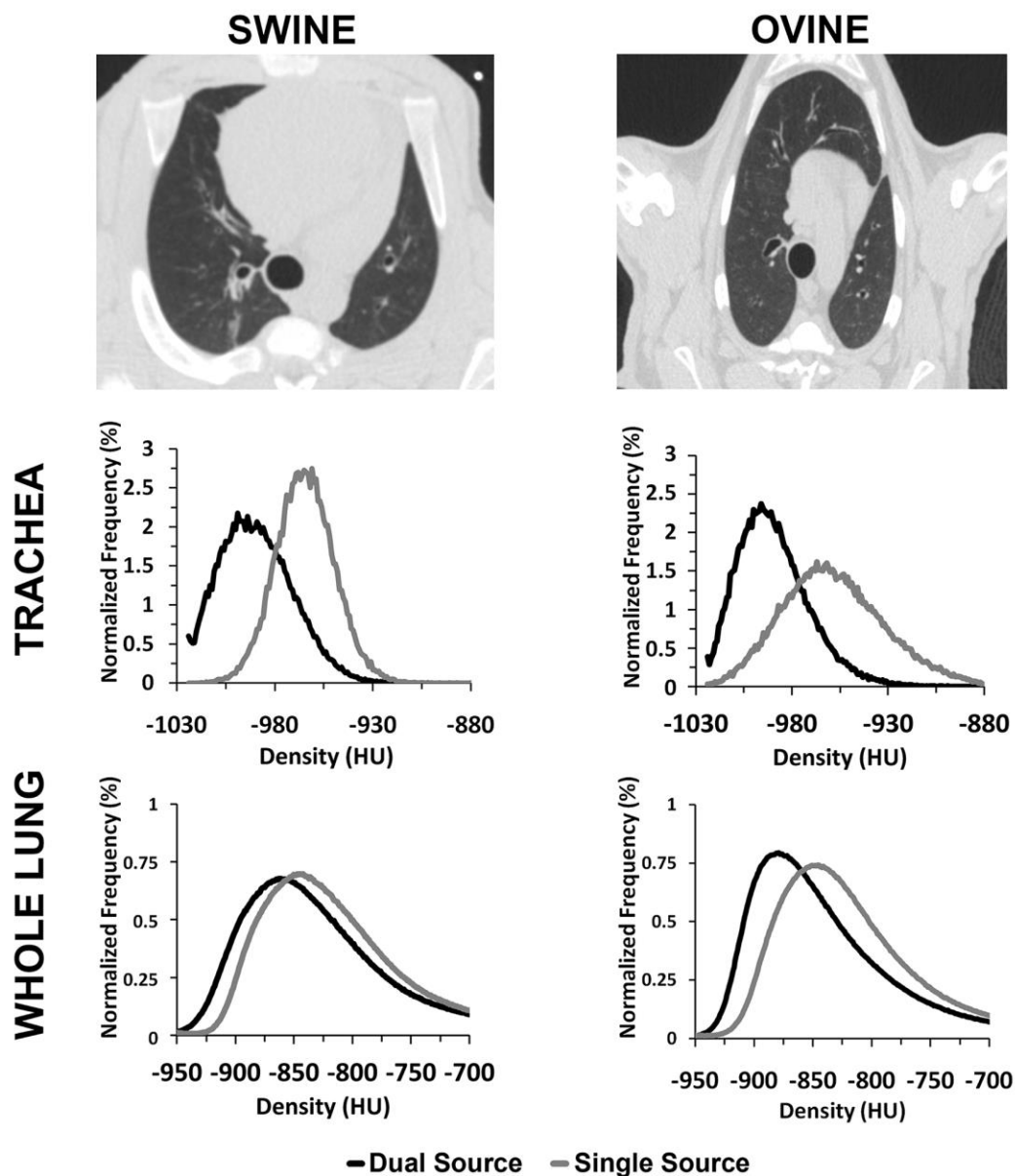
Figure 7. Swine (*top-left panel*) have a more vertically dimensioned thorax compared to the more human-like thorax present in ovine (*top-right panel*). A positive HU shift is present in the histograms of both the trachea (32-35 HU, *middle row*) and whole lung regions (10-12 HU, *bottom row*) between SS and DSDE modes. The normalized density histograms shown are derived from 140 kVp scans from example animals.
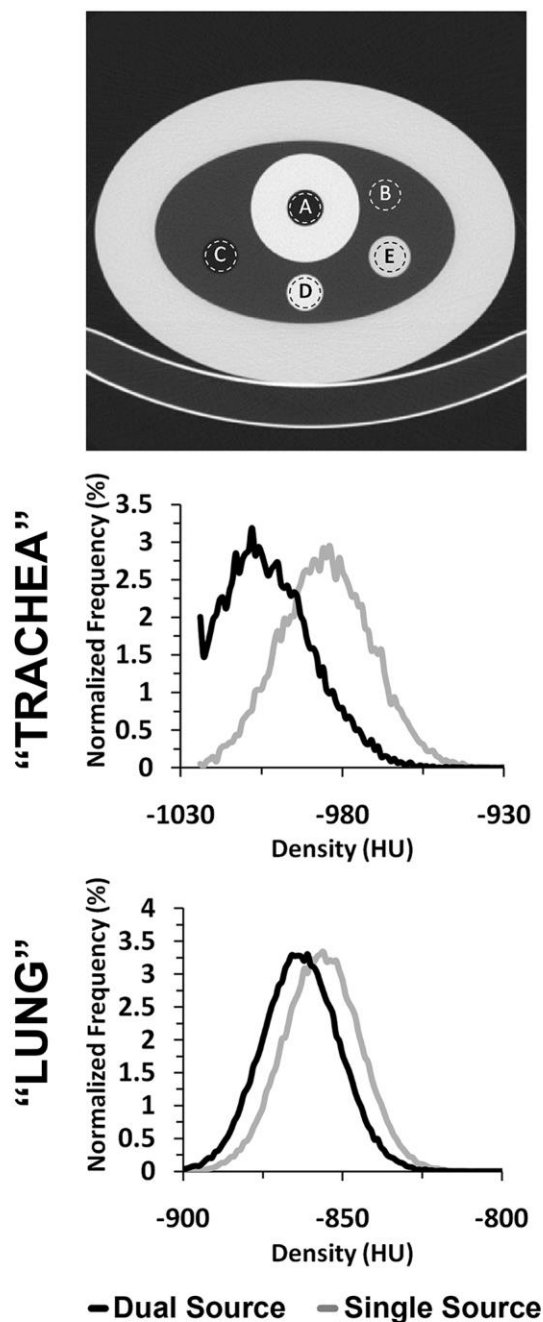
Figure 8. A variant of the COPDGene phantom (*top panel*), with regions representative of the trachea (*A*), lung parenchyma (*B*), air (*C*), acrylic (*D*), and water (*E*), was scanned in SS, DSDE and DSDE-SS modes at 80, 100 and 140 kVp. A HU shift between SS and DSDE modes is demonstrated in the histograms of both the "tracheal" (26 HU, *middle panel*) and the "lung" regions (10 HU, *lower panel*). The normalized density histograms shown are derived from SS and DSDE 140 kVp scans. Similar shifts are also seen in the 80 and 100 kVp scans.
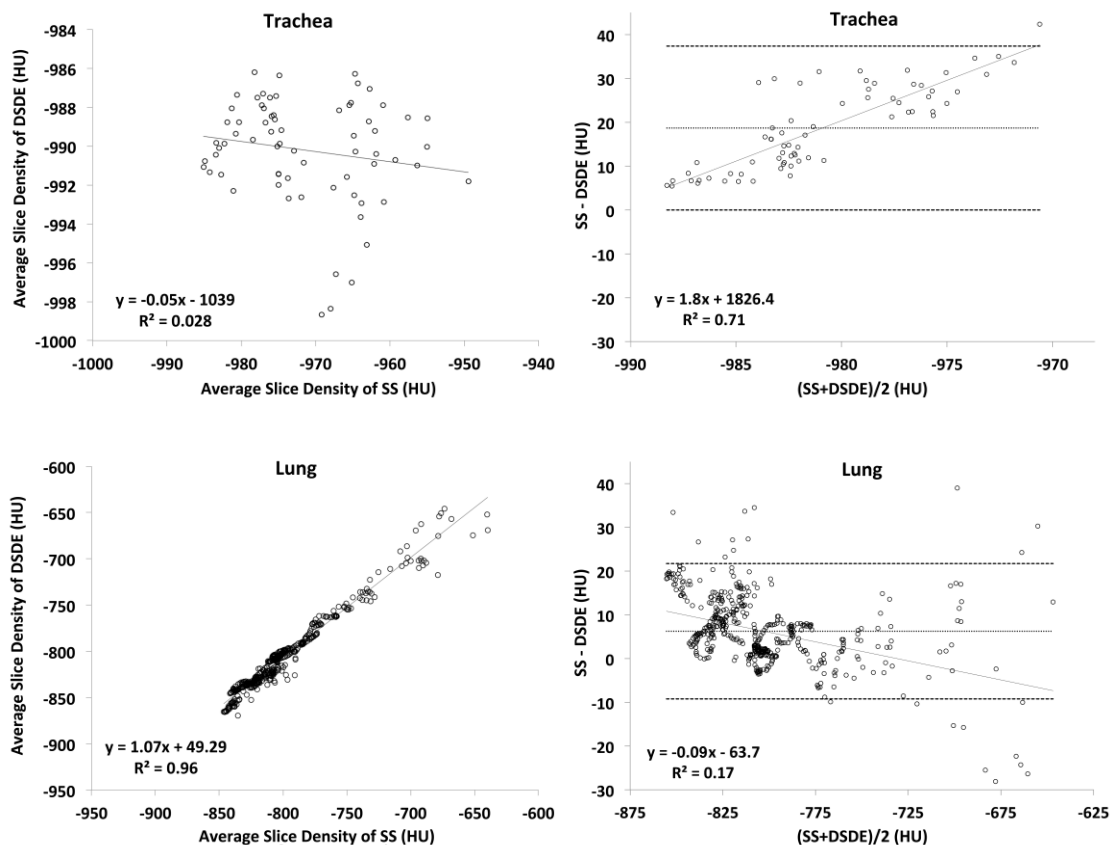
Figure 9. Linear regression plots of average slice densities comparing SS and DSDE at 80 kVp are shown for the in-vivo trachea (*top, left-panel*) and lung parenchyma (*bottom, left-panel*) from an example swine. Similarly, Bland-Altman plots show the relationship of the mean of the average slice densities from the SS and DSDE scans vs. the difference between values obtained from the two scanning modes operated at 80 kVp. Data obtained from the trachea (*top, right-panel*) and lung parenchyma (*bottom, right-panel*) of the same swine as depicted in the left panels.
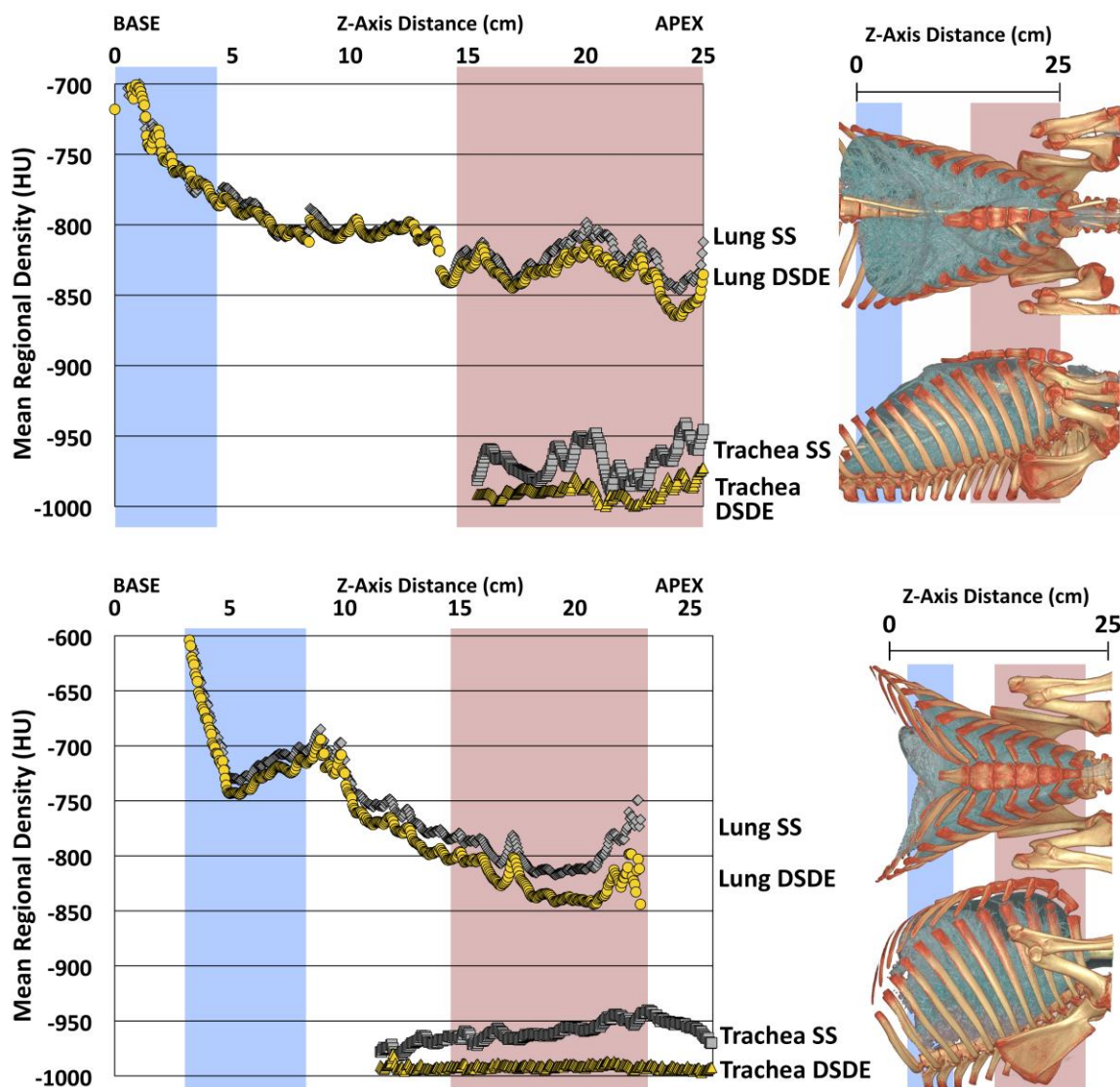
Figure 10. Mean of tracheal and lung HU values along the z-axis from SS and DSDE (80 kVp) scans SS data are in grey and DSDE are in yellow for an example swine (*top*) and ovine (*bottom*). Anatomical reference volume rendered images (*right panel*) in the dorsal-ventral and lateral projections of the swine (*top*) and ovine (*bottom*) are provided to demonstrate the anatomic basis for the SS-DSDE differences. Color coded background bars are provided to help link the anatomic locations to the positions on the density graphs. Note that SS vs. DSDE difference in the trachea are reflected in the lung and the greatest SS vs. DSDE differences in both the lung and tracheal regions occur in an anatomic location associated with the sternum and scapula regions.
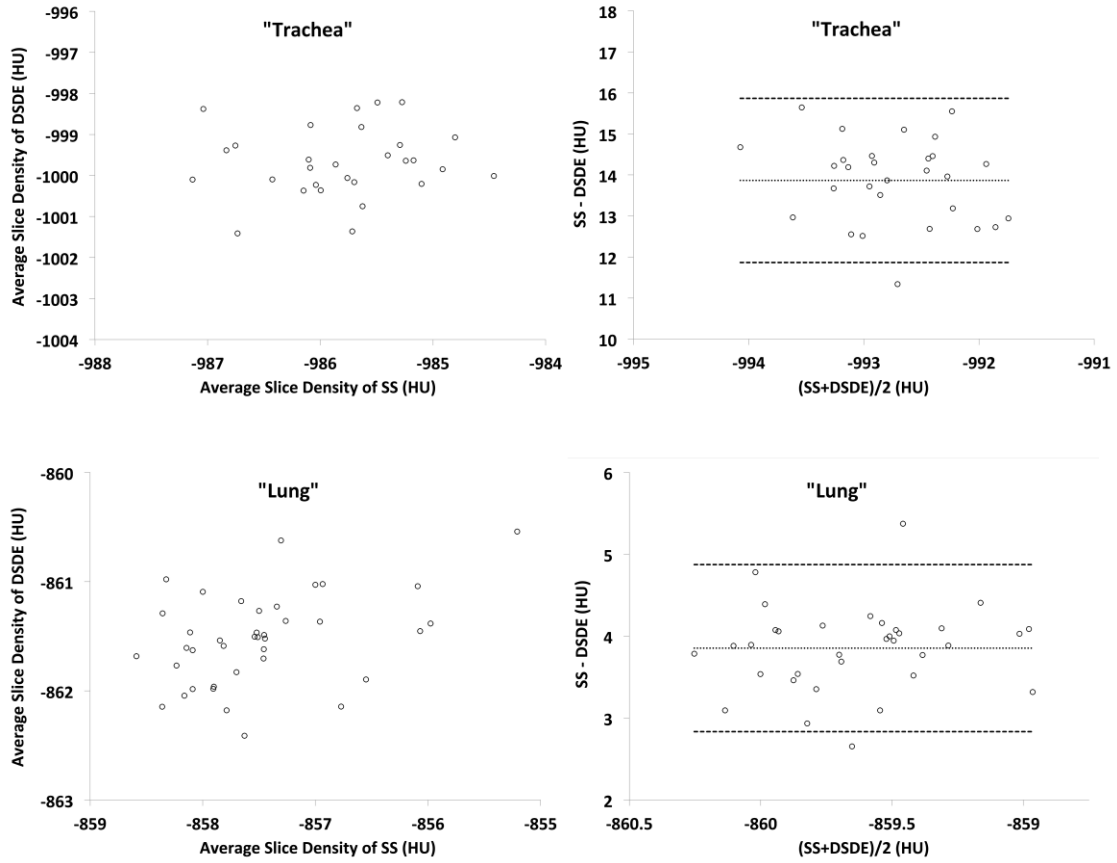
Figure 11. These plots are similar to those shown in **Figure 9** but are derived from a variant of the COPDGene Phantom.

Table 1. HU values, paired differences and significance tests, from 80 kVp scans of multiple subjects, with all scanning parameters matched, except for scan mode (SS vs DSDE) which is being compared.

		Swine		Ovine	
		SS	**DSDE**	**SS**	**DSDE**
Trachea	**Mean**	-949	-981	-954	-986
	|Difference| ± SD	32 ± 6		32 ± 7	
	T-Test	*p* < 0.001 (*n*=18)		*p* < 0.001 (*n*=12)	
Lung	**Mean**	-709	-733	-773	-794
	|Difference| ± SD	24 ± 15		19 ± 5	
	T-Test	*p* < 0.001 (*n*=18)		*p* < 0.001 (*n*=12)	
IVC	**Mean**	24	39	23	37
	|Difference| ± SD	15 ± 1.6		14 ± 1.5	
	T-Test	*p* < 0.001 (*n*=18)		*p* < 0.001 (*n*=12)	

Table 2. A variant of the COPDGene phantom (**Fig. 8**, *top panel*), with "trachea" and "lung" like regions as well as air, water, and acrylic regions, is scanned to compare SS and DSDE modes.

		80 kVp		140 kVp	
		SS	**DSDE**	**SS**	**DSDE**
"Trachea"	**Mean**	-987	-1003	-987	-1004
	|Difference| ± **SD**	16 ± 2		17 ± 2	
	T-Test	*p* < 0.001 (*n*=10)		*p* < 0.001 (*n*=10)	
Air	**Mean**	-999	-1002	-998	-1004
	|Difference| ± SD	3 ± 4		6 ± 2	
	T-Test	*p* < 0.05 (*n*=10)		*P* < 0.001 (*n*=10)	
"Lung"	**Mean**	-858	-860	-856	-863
	|Difference| ± **SD**	2 ± 5		7 ± 3	
	T-Test	*p* = 0.1701 (*n*=10)		*p* < 0.001 (n = 10)	
Water	**Mean**	-2	2	-2	2
	|Difference| ± **SD**	4 ± 8		4 ± 6	
	T-Test	*p* = 0.1816 (*n*=10)		*p* = 0.0972 (*n*=10)	
Acrylic	**Mean**	94	111	125	154
	|Difference| ± **SD**	17 ± 15		29 ± 8	
	T-Test	*p* < 0.01 (*n*=10)		*p* < 0.001 (*n*=10)	

Note: Reference CT number for internal "trachea" air is -1000 HU; internal air is -1000 HU; "lung" is -860 HU; water is 0 HU; acrylic is 120 HU (the material is dependent on the photon energy spectrum).

Table 3. CT numbers from the "trachea" like region of a variant of the COPDGene phantom under multiple scan settings.

	Scan Mode	Mean	Channels	Pitch	Rot. Time	Kernel	Tube	Sn filtered
80 kVp	SS	-987	128	0.55	0.5	B35f	A	-
	DSDE-SS	-1002	64	0.55	0.5	B35f	A	-
	DSDE-SS	-1002	128	0.55	0.5	B35f	A	-
	DSDE	-1002	128	0.55	0.5	B35f	A	-
	DSDE	-1002	128	1.0	0.5	B35f	A	-
	DSDE	-1001	128	0.55	0.33	B35f	A	-
	DSDE	-1003	128	0.55	0.5	D30f	A	-
	DSDE-SS	-1003	64	0.55	0.5	B35f	B	-
	DSDE-SS	-1004	128	0.55	0.5	B35f	B	-
	DSDE	-1003	128	0.55	0.5	B35f	B	-
	DSDE	-1002	128	1.0	0.5	B35f	B	-
	DSDE	-1003	128	0.55	0.33	B35f	B	-
	DSDE	-1002	128	0.55	0.5	D30f	B	-
100 kVp	SS	-988	128	0.55	0.5	B35f	A	-
	DSDE-SS	-1004	64	0.55	0.5	B35f	A	-
	DSDE-SS	-1007	128	0.55	0.5	B35f	A	-
	DSDE	-1002	128	0.55	0.5	B35f	A	-
120 kVp	SS	-985	128	0.55	0.5	B35f	A	-
140 kVp	SS	-987	128	0.55	0.5	B35f	A	-
	DSDE-SS	-1002	64	0.55	0.5	B35f	A	-
	DSDE-SS	-1007	128	0.55	0.5	B35f	A	-
	DSDE	-1002	128	0.55	0.5	B35f	A	-
	DSDE-SS	-1000	64	0.55	0.5	B35f	B	yes
	DSDE-SS	-1001	128	0.55	0.5	B35f	B	yes
	DSDE	-1003	128	0.55	0.5	B35f	B	yes

Table 4. CT numbers from the "trachea" like region of a modified COPDGene phantom under multiple scan settings.

Phantom "Trachea" values					
	Scan Mode	Mean	Slice Thickness	Slice Spacing	Scan Direction
80 kVp	SS	-975	0.6	0.5	Cranio-caudal
	DSDE-SS	-1002	0.6	0.5	Cranio-caudal
	DSDE-SS	-1001	0.75	0.5	Cranio-caudal
	DSDE-SS	-1002	0.6	0.6	Cranio-caudal
	DSDE-SS	-1002	0.6	0.5	Caudal-cranial
140 kVp	SS	-974	0.6	0.5	Cranio-caudal
	DSDE-SS	-1002	0.6	0.5	Cranio-caudal
	DSDE-SS	-1001	0.75	0.5	Cranio-caudal
	DSDE-SS	-1001	0.6	0.6	Cranio-caudal
	DSDE-SS	-1002	0.6	0.5	Caudal-cranial

CHAPTER 4: QUANTITATIVE ASSESSMENT OF WATER, AIR, TRABECULAR BONE, AND BLOOD MEASURES IN DUAL-SOURCE COMPUTED TOMOGRAPHY

Introduction

All modern clinical CT scanners are calibrated with the goal of scaling CT numbers of water to be 0 HU and CT numbers of air close to be -1000 HU at all kVp values. However, this calibration is performed under ideal scanning conditions (e.g., using a cylindrical water phantom and in-air assessed at the scanner isocenter). Under realistic scanning conditions, many confounding factors (e.g., scatter, beam hardening, etc.) interfere and, if not fully compensated, can cause significant deviations of the CT numbers from their nominal values. Therefore, a proper compensation of scatter, beam hardening and other common artifacts is of considerable importance for QCT imaging of the lungs. In this study, we focus on the potential effect of dedicated scatter correction techniques implemented in dual-source CT (DSCT) scanners has on the quantification of bone and fluids in and near the thorax of an anatomically accurate "phantom" model.

The motivation for this study stems from our observations in animal experiments that air in the trachea was consistently closer to -1000 HU when using the DSDE mode compared to the SS mode of the Definition Flash scanner (chapter 3). To determine if this shifting was isolated to air, we tested the hypothesis that the dedicated scatter-correction employed in the DSDE mode results in more accurate (closer to the nominal 0 HU) CT numbers of water in and around the thorax compared to the SS mode representing conventional single-source CT. In addition to internal and external water measures, regions including trabecular bone, the inferior vena cava (IVC) and internal and external

air measures were acquired to provide a more robust understanding of quantitation in modern CT imaging.

Materials and Methods

The Institutional Animal Care and Use Committee approved all animal studies reported here. Two farm-bred swine (37.1, 39.3 kg; 1 female) were premedicated with Ketamine (20 mg/kg) and Xylazine (2 mg/kg) intramuscularly, and anesthetized with 3–5% isoflurane in oxygen by nose cone inhalation. Once surgical depth of anesthesia was achieved, an 8.0-mm inner diameter cuffed endotracheal tube was placed through a tracheostomy and the animals were mechanically ventilated with 100% oxygen, tidal volume of 10-14 mL/kg, rate of 10-20 breaths/min adjusted to achieve an end-tidal PCO_2 of 30–40 mm Hg. Carotid arterial and external jugular venous introducers were placed. Surgical plane of anesthesia was maintained with inhaled isoflurane (1–5% in oxygen), neuromuscular blockade was achieved with pancuronium (0.1 mg/kg IV initial dose and 0.5–1 mg/kg hourly as needed). Arterial pressure, oxygen saturation, and airway pressures were continuously monitored and recorded. Animals were placed supine on the scanner table and were held with gentle forelimb traction. Consistent static breath-holds were achieved through the use of an adjustable water column positioned next to the scanner, to provide 20 cmH_2O airway pressure during the breath-hold with a flow through of 3-5 L/min of room air to maintain backpressure, connected to the proximal end of the endotracheal tube.

At the conclusion of scanning, the deeply anesthetized animals were euthanized, an incision was made substernal, and a 60cc syringe filled with water was inserted into the thoracic cavity and secured to the sternum near the heart. An additional 60cc water

filled syringe was secured to the external chest wall. This effectively created an experimental animal "phantom" (**Fig. 12**) which maintains major anatomic structure and is used to determine the effects of scatter correction on water within the thorax.

All imaging was performed on a second-generation dual-source CT scanner (Somatom Definition Flash, Siemens Medical Systems, Erlangen, Germany). Animals were scanned in the SS mode (80, 140 kVp), and in the DSDE mode (80/140Sn kVp and 140/80 kVp) while exploring the effect, if any, of varying available scanning parameters. Such parameters included rotation time (0.33 or 0.5s); pitch (0.55 or 1.0); detector collimation (64 or 128); and reconstruction kernel (B35f or D30f). A consistent $CTDI_{vol}$ of 12 (+/- 0.1)mGy was used for all scans, except the dose controlled scans which had a $CTDI_{vol}$ of 6 (+/- 0.1)mGy. Each CT scan on the animal "phantom" was repeated 10 times to provide a more robust statistical analysis.

Scans were reconstructed, transferred to local database, and analyzed using the Pulmonary Analysis Software Suite (PASS) image analysis software (49). The animal "phantom" was manually segmented into six distinct regions of interest (internal and external air, internal and external water, trabecular bone of the T7 vertebrae, and the IVC as illustrated in **Fig. 12**), being careful to avoid any partial volume effect from wall and edge regions. Voxel densitometry measures of mean, median, mode, and standard deviation were then recorded along with histogram results. Scans of the live animal models were segmented using semi-automated airway and whole lung algorithm. To ensure that only lung tissue was used in voxel densitometry calculations for the whole lung in the live animals, resultant segmentations from PASS were eroded to minimize contamination by the chest wall and mediastinum. Histogram analysis was performed on

the regions of interest to quantify regions and illustrate shifts. Two-tailed paired difference t-tests were performed on each data set of the animal "phantom" to determine the quantitative significance of HU differences when comparing SS and DSDE modes.

Results

Similar to the tracheal experiments (chapter 3), a shift between the HU values derived from the SS and DSDE modes (**Fig. 13**) was observed in the whole lung region of swine (**Fig. 13**, *top panel*), with the DSDE scans producing CT numbers which are more negative than their SS counterpart. However, when looking at histogram peaks in more dense regions (i.e. peaks near and above 0 HU), a detectable shift (14 HU) in the opposing direction is observed at the peak (**Fig. 13**, *bottom panel*).

The animal "phantom" with water inserts demonstrated HU shifts of varying magnitudes and directions for different objects, and with DS mode being more accurate at deriving water CT numbers than SS mode, regardless of location (**Table 5**). For example, at 80 kVp: the derived values for water inside the thorax are -6.5 ($\pm$ 1.8) HU in SS mode and 0.6 ($\pm$ 3.0) HU in DSDE mode; in water outside the thorax, the SS and DSDE values are -9.5 ($\pm$ 1.1) HU and -2.3 ($\pm$ 3.0) HU respectively.

Use of the tin filter on tube B for 140 kVp scans accounted for only a very small and insignificant variance in CT numbers in the analyzed materials (**Table 5**). Any deviation between the with- and without- filter scans was probably caused by difference in beam hardening (additional tin filter makes the X-ray spectrum harder) and does not account for the marked quantitative differences between DSDE and SS scans.

The observed DSDE vs. SS behavior for water remained similar across all acquisition/reconstruction parameters used in the experiment (**Table 6**). Within SS scans

there is a measurable shift in the value of water based on its location in or near the thorax. This is not seen in DSDE scans where the value for water inside the thoracic cavity is consistent with its measured value on the outside of the thorax at a given energy (**Table 5**).

Standard deviation (image noise) in the DSDE mode was consistently higher than in the SS mode. This is expected because matching $CTDI_{vol}$ between the DSDE and SS modes resulted in much lower dose per tube for the DSDE mode because the $CTDI_{vol}$ is split between the two tubes. Noise was the highest when using DSDE mode with a reduced $CTDI_{vol}$.

In the DSDE mode, values derived from the images reconstructed with the B35f and D30f kernels were very similar (**Table 6** and **7**). This is not very surprising since the B35f and D30f kernels have similar (medium strength) sharpness and no edge enhancement. The edge enhancement feature can modify CT numbers in the edge vicinity and, hence, affect the accuracy of CT numbers.

DSDE values acquired from scans taken with rotation times of 0.33s and 0.5s were almost identical (**Table 6** and **7**). This is expected as the scan helices have the same coverage of the object. In scans comparing the effect of pitch, a pitch of 1.0 produced more noise compared to a pitch of 0.55. Again, this is expected since increasing the pitch by increasing the table speed reduces scanning time, but at the cost of decreased image resolution since the coverage of the detector system is lower.

The IVC displayed similar CT number characteristics to water in these experiments. Mean values in the IVC for the SS and DSDE control were 35 ($\pm$ 2.3) HU

and 49 (± 4.1) HU respectively at 80 kVp and were similar for 140 kVp scans (**Table 7**). Literature values for blood are typically referenced as 50-60 HU.

The air inside the thoracic cavity demonstrated similar, however less pronounced, shifting in values from SS to DSDE mode as seen in chapter 3. Mean values of air inside the cavity were -955.6 (± 1.1) in SS mode at 80 kVp and -973.4 (± 2.8) HU in DSDE mode at 80 kVp (**Table 7**). These values differed slightly in 140 kVp scans where the values were -959.8 (± 1.7) HU in SS mode and -992.5 (± 1.8) HU in DSDE mode (**Table 7**).

<u>Discussion</u>

Our studies indicate that the Definition Flash scanner provided more accurate and consistent measures CT numbers of water within and near the thorax when the scanner was operated in the DSDE mode. A negative shift of up to 11 HU in water and 14 HU in the IVC of the animal "phantom" experiment was observed, when the scanner was operated in the SS mode representing scanning similar to that used in a conventional single-source CT.

As discussed in chapter 3, the beam hardening correction method in the Definition Flash scanner is the same for both SS and DSDE modes of operation. On the other hand, the scatter correction techniques are different between the two modes. Therefore, the results of this study suggest that the dedicated scatter correction technique employed by the Definition Flash, as discussed by Petersilka et al. (67) in the DSDE mode plays a major role in generating more accurate CT numbers, not only for tracheal air, but for fluids within the thorax.

The improved accuracy of air and water CT numbers is of great importance for QCT imaging. Because our results suggest that scatter correction serves to correct air, water and blood values within the animal "phantom" scan we further support our conjecture that non-ideal compensation of forward-scattered radiation is likely a major factor responsible for the deviation of CT numbers from their nominal values.

The results of our study suggest that non-ideal compensation of forward-scattered radiation is a major factor responsible for the deviation of air CT numbers from the nominal value of -1000 HU. Therefore, we believe that QCT lung imaging can potentially benefit from dedicated forward-scatter correction techniques which could be either model-based (93) or measurement-based (94, 95).

In conclusion, our study suggests that the enhanced scatter correction technique employed by the DSDE mode of a second generation DSCT scanner results in more accurate CT numbers of air, water and blood compared to the SS mode representing conventional single-source CT.
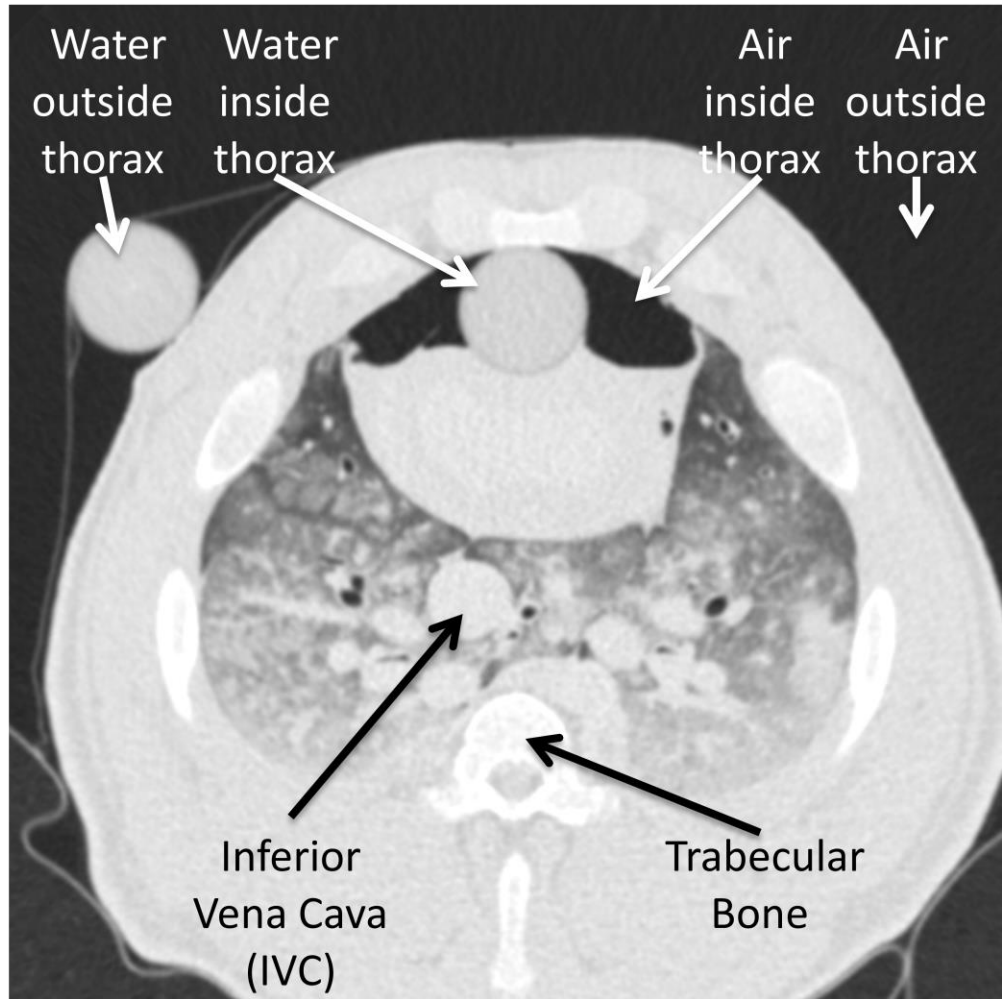
Figure 12. An animal "phantom" was created from the thorax of a euthanized swine. Measured regions consisted of a water filled 60cc syringe that was secured to the outer wall of the chest (*water outside thorax*), a water-filled syringe secured to the inside the thoracic cavity along the sternum (*water inside thorax*), the air within the thoracic cavity (*air inside thorax*), the air external to the thorax (*air outside* thorax), the inferior vena cava (IVC) (*inferior vena cava*), and trabecular vertebral bone (*trabecular bone*).
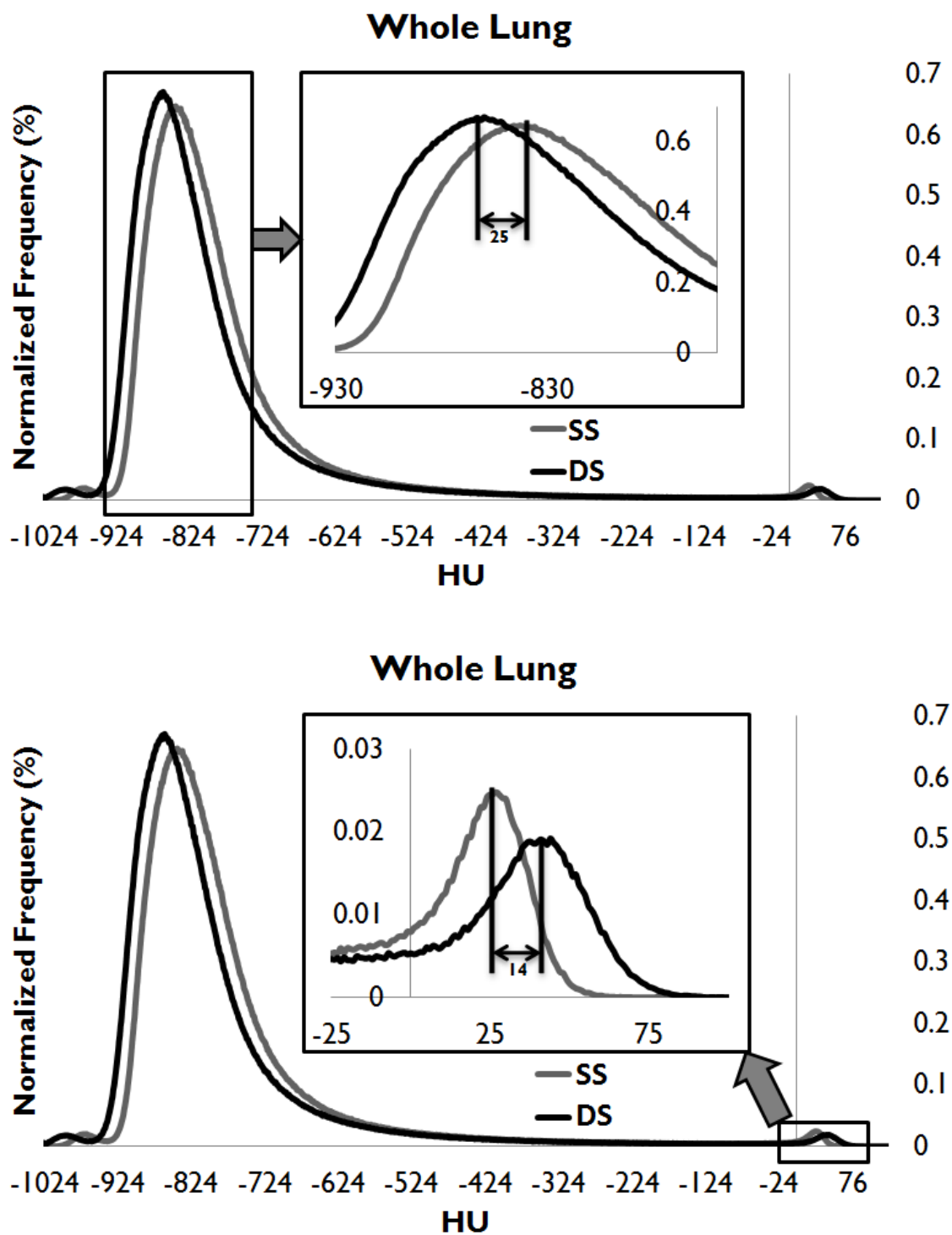
Figure 13. The normalized density histograms shown are derived from 80 kVp scans from a representative swine. A positive HU shift is present in the lung parenchyma (25 HU, *top row*) and a negative HU shift is present in the fluid and vasculature (14 HU, *bottom row*) between SS and DSDE modes.

Table 5. CT number comparison in multiple ROIs in the animal "phantom" (**Fig. 13**).

		80 kVp		140 kVp		
				with Sn filter		no filter
		SS	DS	SS	DS	DS
Water Inside Thorax	**Mean**	7	1	2	3	3
	|Difference| ± SD	6 ± 4		1 ± 2		
	T-Test	$p < 0.001$ (n=10)		$p = 0.1582$ (n=10)		
Water Outside Thorax	**Mean**	-10	-2	-9	8	7
	|Difference| ± SD	7 ± 3		17 ± 2		
	T-Test	$p < 0.001$ (n=10)		$p < 0.001$ (n=10)		
IVC	**Mean**	35	49	36	46	46
	|Difference| ± SD	14 ± 3		10 ± 3		
	T-Test	$p < 0.001$ (n=10)		$p < 0.001$ (n=10)		
Trabecular Bone	**Mean**	345	331	227	208	210
	|Difference| ± SD	15 ± 5		19 ± 4		
	T-Test	$p < 0.001$ (n=10)		$p < 0.001$ (n=10)		
Air Inside Thorax	**Mean**	-956	-974	-960	-993	-993
	|Difference| ± SD	18 ± 3		33 ± 2		
	T-Test	$p < 0.001$ (n=10)		$p < 0.001$ (n=10)		
Air Outside Thorax	**Mean**	-999	-994	-998	-1002	-1001
	|Difference| ± SD	6 ± 2		4 ± 1		
	T-Test	$p < 0.001$ (n=10)		$p < 0.001$ (n=10)		

Note: The reference CT number for internal and external water is 0 HU; internal and external air is -1000 HU; IVC is 50-60 HU; bone is >100 HU and dependent on the photon energy spectrum and type of bone.

Table 6. CT number comparison at multiple scan settings for water inside the thorax, water outside the thorax, and inferior vena cava (IVC) in the animal "phantom" (**Fig. 13**).

	Scan Mode	80 kV Mean (HU)	140 kV Mean (HU)	CTDI$_{vol}$ (mGy)	Channels	Kernel	Rotation Time (s)	Pitch
Swine "Phantom" values								
Water Inside Thorax	SS	7	2	12	128	B35f	0.33	0.55
	DSDE	1	3	12	128	B35f	0.33	0.55
	DSDE	2	2	6	128	B35f	0.33	0.55
	DSDE	2	0	12	64	B35f	0.33	0.55
	DSDE	2	3	12	128	D30f	0.33	0.55
	DSDE	0	5	12	128	B35f	0.5	0.55
	DSDE	1	2	12	128	B35f	0.33	1.0
Water Outside Thorax	SS	-10	-9	12	128	B35f	0.33	0.55
	DSDE	-2	8	12	128	B35f	0.33	0.55
	DSDE	-3	10	6	128	B35f	0.33	0.55
	DSDE	-1	9	12	64	B35f	0.33	0.55
	DSDE	0	9	12	128	D30f	0.33	0.55
	DSDE	-1	11	12	128	B35f	0.5	0.55
	DSDE	-2	8	12	128	B35f	0.33	1.0
Inferior Vena Cava (IVC)	SS	35	36	12	128	B35f	0.33	0.55
	DSDE	49	46	12	128	B35f	0.33	0.55
	DSDE	48	47	6	128	B35f	0.33	0.55
	DSDE	52	47	12	64	B35f	0.33	0.55
	DSDE	48	47	12	128	D30f	0.33	0.55
	DSDE	49	45	12	128	B35f	0.5	0.55
	DSDE	49	47	12	128	B35f	0.33	1.0

Table 7. CT number comparison at multiple scan settings for trabecular bone, air inside the thorax, and air outside the thorax in the animal "phantom" (**Fig. 13**).

	Scan Mode	80 kV Mean (HU)	140 kV Mean (HU)	CTDI$_{vol}$ (mGy)	Channels	Kernel	Rotation Time (s)	Pitch
					Swine "Phantom" values			
Trabecular Bone	SS	345	227	12	128	B35f	0.33	0.55
	DSDE	331	208	12	128	B35f	0.33	0.55
	DSDE	332	208	6	128	B35f	0.33	0.55
	DSDE	332	210	12	64	B35f	0.33	0.55
	DSDE	330	207	12	128	D30f	0.33	0.55
	DSDE	331	208	12	128	B35f	0.5	0.55
	DSDE	332	209	12	128	B35f	0.33	1.0
Air Inside Thorax	SS	-956	-960	12	128	B35f	0.33	0.55
	DSDE	-973	-993	12	128	B35f	0.33	0.55
	DSDE	-972	-994	6	128	B35f	0.33	0.55
	DSDE	-973	-992	12	64	B35f	0.33	0.55
	DSDE	-972	-995	12	128	D30f	0.33	0.55
	DSDE	-972	-994	12	128	B35f	0.5	0.55
	DSDE	-972	-993	12	128	B35f	0.33	1.0
Air Outside Thorax	SS	-999	-998	12	128	B35f	0.33	0.55
	DSDE	-994	-1002	12	128	B35f	0.33	0.55
	DSDE	-995	-1003	6	128	B35f	0.33	0.55
	DSDE	-994	-1001	12	64	B35f	0.33	0.55
	DSDE	-996	-1004	12	128	D30f	0.33	0.55
	DSDE	-996	-1003	12	128	B35f	0.5	0.55
	DSDE	-996	-1002	12	128	B35f	0.33	1.0

CHAPTER 5: CONCLUSION

This work demonstrates the importance of scatter correction for accurate CT-based assessment of intrathoracic air which is used in the assessment of the presence and distribution of emphysema associated with COPD. By utilizing the newly implemented scatter correction on a Definition Flash scanner to demonstrate that well recognized shifts in HU for tracheal air along with lung parenchyma, blood and water can be significantly reduced if not eliminated. While inadequate scatter and beam hardening corrections are both contenders for causing the shifts in HU within low-density intrathoracic regions, beam-hardening corrections remained the same between scanner modes used in this study while scatter correction changed between single source and dual-source scanning modes. In the dual-source modes, intrathoracic structures were more accurately represented by the reconstructed HUs.

This work shows the importance of anatomical structure in quantitative imaging. In chapter 3, it is shown that as surrounding bone structure becomes more dense and complex, the tracheal air CT number variation becomes more pronounced when the improved scatter correction techniques are not incorporated. When the new scatter correction techniques are comprised in the imaging, there is very little variation in tracheal air values seen as the thorax anatomy changes.

This work serves to show that the implementation of improved scatter correction techniques can significantly reduce the HU shifts in lung density metrics, a shift that has challenged the efforts to use quantitative CT in the phenotyping of COPD. We furthermore demonstrate that efforts to use a mean value of tracheal air to correct lung

density values retrospectively are not likely to be successful, even for the purposes of normalizing data between scanners.

With QCT taking center stage in the quest to phenotype the lung in terms of presence, distribution and progression of emphysema, the findings presented in this work is of considerable importance to the imaging community.

Bearings On QCT

The accuracy of air and water CT numbers is of particular importance for QCT imaging, as it is the bases for all measurements along with volume. Through improved accuracy of lung CT density measures, QCT can provide a more accurate assessment of the presence, severity and development of pathologies. Thus, delivers a more exact means of phenotyping patients for a more accurate, patient centric treatment plan. This body of work has sought to characterize *in vivo* and phantom-based air and water metrics using dual-source, dual-energy computed tomography technology where the nature of the technology has required adjustments to scatter correction.

One of the major issues in QCT imaging is the production of reliable, repeatable, and accurate quantification of volumetric CT data for assessment of lung density. This is of particular challenge in longitudinal and multi-center studies where we have seen variability of intrathoracic air measures across sites and manufacturers (**Fig. 14**). This variability limits accuracy of emphysema and air trapping measures and makes comparison between CT scanner make and models difficult. By providing air density measures in the thorax reliably closer to that of -1000 HU, new scatter correction techniques associated with DSDE CT may ultimately provide better uniformity in density measures across sites.

The quantitative accuracy provided by next generation scatter correction techniques in deriving endotracheal air and intrathoracic water CT numbers that are closer to their theoretical values -- which is presented in this work -- is a critical element in establishing the efficiency of longitudinal assessments. There has been increasing interest in using pulmonary biomarkers to understand and monitor respiratory disease. QCT measures fit the NIH definition of a biomarker as "a characteristic that is objectively measured and evaluated as an indicator of normal biological processes, pathogenic processes, or pharmacological responses to a therapeutic intervention" (97, 98). As new scanners allow for more reliable and accurate quantification, additional metrics can be better utilized and developed to provide a new array of potential biomarkers capable of detecting pathologies, tracking disease progression, and tracking therapeutic response.

For example, the deviation in CT numbers from "true" water and air values in traditional single-source scanners -- particularly in the apical regions of the thorax where scapular, sternal and spinal structures converge -- indicate that patient lung prognosis currently based on SS QCT evaluation may be skewed by scatter.

Also of major importance in QCT is noise level. There are many tradeoffs in image quality, and many times the different image quality characteristics are interrelated. The signal-to-noise ratio (SNR) in imaging may be affected by many different confounding factors, including but not limited to pitch and dose, causing a loss in image quality. In addition, the sharpness of a volume may be affected by kernel type and other post processing factors and may be improved by new iterative reconstruction techniques such as the proprietary iterative reconstruction in image space (IRIS) and now sinogram

affirmed iterative reconstruction (SAFIRE) which has been developed to compensate for the noise generated in low patient dose scans.

The sharpness of an image can have a noticeable effect on voxel percentile and HU cutoff criteria currently used in quantifying air trappings and extent of emphysema-like parenchyma. These measures have been defined as the percentage of voxels below a certain HU threshold or percentile. In images containing a higher amount of noise, the distributions of measured values begin to widen, i.e. the peaks are less sharp. For illustrative purposes, **Figure 15** has been included and shows the voxel index value of -910 HU used by some groups to quantify emphysema progression (99). This demonstrates that an image with higher variance can include a higher amount of voxels below a given threshold, even though the mean values in the volumes are approximately equivalent.

Noise can have an effect on airway wall area measures, which is an independent metric of airflow obstruction in COPD (100). Research has demonstrated that there is a fractional error in the estimation of airway wall and lumen area in small airways in measurements derived from CT, compared with histological analysis (101, 102), and is in part due to a systematic overestimation of wall area and underestimation of lumen in CT analysis (103). This error is attributed, in part, to noise associated with high special resolution scanning (103, 104). The more accurate assessment of CT numbers for air within the lung provided by scatter correction, as shown in this work, can also potentially provide more accurate FWHM airway thickness analysis (105).

There are tradeoffs between image quality and radiation dose. In clinical lung imaging they require a high SNR for solid nodule detection and identification of

emphysema (106, 107). We demonstrate in both chapters 3 and 4, through variations in scanning parameters, that the most important noise parameters in helical, DSDE CT imaging are dose and pitch.

As described in chapter 2, image noise is proportional to square root of dose. E.g. if the dose (in mAs, or effective mAs) of a given scan is doubled, then the noise is expected to decrease by 0.707 (29% decrease). Conversely, if the dosage is reduced to ½ of the original, then the noise is expected to increase by 1.41 (41% increase). This very closely matches the changes in standard deviation values measured in this work.

<u>Limitations and Further Work</u>

In our studies we only focused on the effect of scatter correction and did not investigate the effect of beam hardening which, for example, is well known to cause significant changes in CT numbers of iodine (96). Such investigation would involve scanning phantoms in a wide size range, while the phantom we used in this study was available only in one size. Nevertheless, no significant difference in the air CT numbers obtained at different tube energies ranging from 80 to 140 kVp, suggest that beam hardening is probably of less importance compared to scatter, at least under conditions of our experiments. Furthermore, because the same beam hardening correction algorithm is used in both DS and SS modes, we felt that the data presented provides the strongest evidence for scatter being the likely source of air value offset in the SS scanning mode.

Another limitation is that we did not use all DS modes available on a Definition Flash scanner. In particular, we did not consider such DS modes as the cardiac and high-pitch ("flash") modes. These modes were excluded because conventional QCT lung imaging is performed using non-cardiac standard-pitch acquisition protocols, while the

cardiac and high-pitch DS modes are prone to additional factors which can compromise the accuracy of air CT numbers. In particular, the cardiac mode is prone to partial scan artifacts, while the high-pitch mode can be affected by more pronounced spiral (windmill) artifacts.

Finally, we did not look into the accuracy of CT numbers in dual-energy post-processed images such as virtual non-contrast (VNC) images obtained by subtracting the contrast signal from contrast-enhanced dual-energy CT lung scans. Dual-energy CT lung imaging is a subject of active research (108, 109). In particular, the use of VNC images for quantitative lung applications is of interest since it can potentially eliminate the need for non-contrast scans and, hence, reduce radiation dose (110). However, a quantitative analysis of VNC lung images is more complicated because it also depends on the parameters used by the DE post-processing algorithm and, hence, this interesting subject deserves more study.

Summary

This body of work has demonstrated CT density measures are more accurately assessed using new scatter correction techniques employed in dual-source modes of the utilized scanner, compared with single source scanners.

With the improved accuracy of lung CT density measures, the use of scatter correction techniques exhibited in this work play important roles, and should be adopted in single source scanners and scanner modes when quantitative CT of the lung is sought.
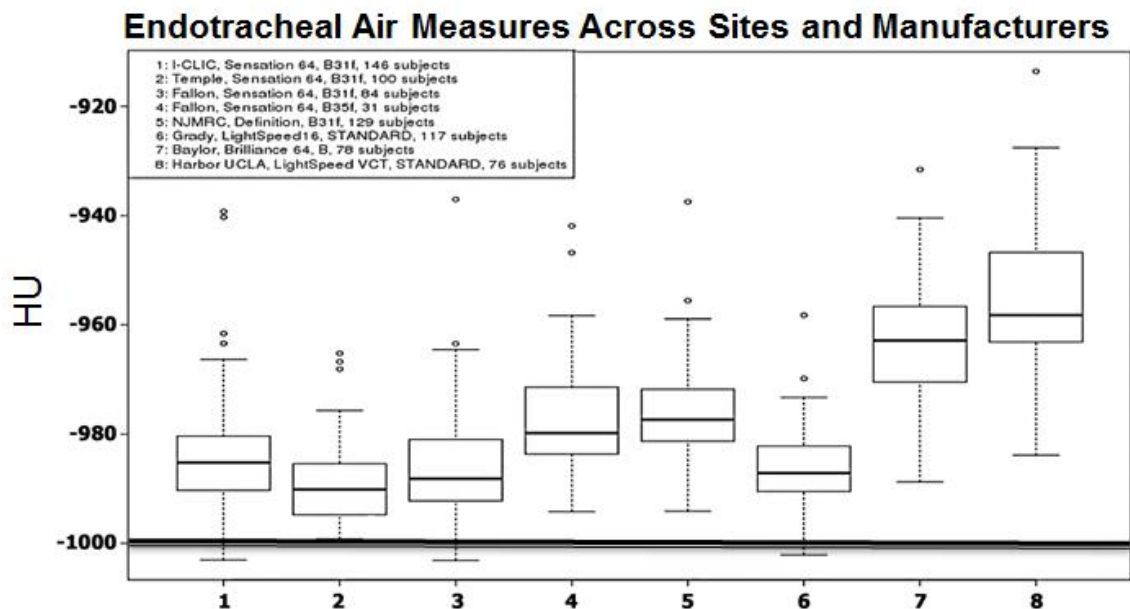
Figure 14. Variability of intrathoracic air HU measures across different sites and manufacturers. This variability limits accuracy of emphysema and air trapping measures and makes comparison between CT scanner make and models difficult. By providing air density measures in the thorax reliably closer to that of -1000 HU, new scatter correction techniques associated with DSDE CT may provide better uniformity in density measures across sites.
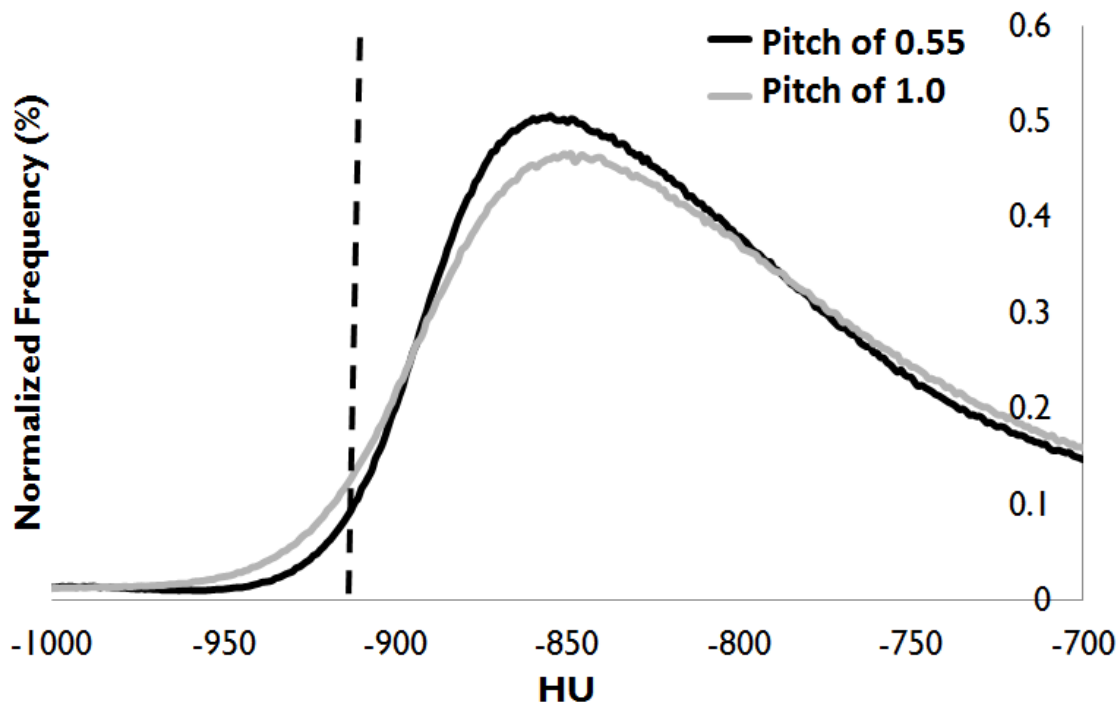
Figure 15. The normalized density histograms of the whole lung from a representative swine as derived from two different pitch settings (0.55 and 1.0) are shown. Both scans have the same effective dose, and are from the 80 kVp tube of a DSDE scan. All other scanning parameters are matched. A higher pitch number is seen to be less sharp and has more noise. A lower pitch is seen to having relatively less noise in the lung parenchyma. The mean values in the volumes are approximately the same, at -811 HU for the 0.55 pitch volume and -810 HU for the 1.0 pitch volume. The dashed line at approximately -910 HU is used to illustrate that the number or percent voxels below a given cutoff (-910 HU in this case) can be changed not just by CT number shifting, but also by image noise. This noise phenomenon is not isolated to variations in pitch, but additional factors including dose, reconstruction kernel, and rotation time.

REFERENCES

1.   Johnson TRC, Krauss B, Sedlmair M, Grasruck M, Bruder H, Morhard D, Fink C, Weckbach S, Lenhard M, Schmidt B, Flohr T, Reiser MF, Becker CR. Material differentiation by dual energy ct: Initial experience. *European radiology* 2007;17:1510-1517.

2.   Michael GJ. Tissue analysis using dual energy ct. *Australasian physical & engineering sciences in medicine / supported by the Australasian College of Physical Scientists in Medicine and the Australasian Association of Physical Sciences in Medicine* 1992;15:75-87.

3.   von Holst H, Li X, Kleiven S. Increased strain levels and water content in brain tissue after decompressive craniotomy. *Acta neurochirurgica* 2012;154:1583-1593.

4.   Svendsen OL, Hassager C, Bergmann I, Christiansen C. Measurement of abdominal and intra-abdominal fat in postmenopausal women by dual energy x-ray absorptiometry and anthropometry: Comparison with computerized tomography. *International journal of obesity and related metabolic disorders : journal of the International Association for the Study of Obesity* 1993;17:45-51.

5.   Hamer OW, Schlottmann K, Sirlin CB, Feuerbach S. Technology insight: Advances in liver imaging. *Nature clinical practice Gastroenterology & hepatology* 2007;4:215-228.

6.   Linguraru MG, Yao J, Gautam R, Peterson J, Li Z, Linehan WM, Summers RM. Renal tumor quantification and classification in contrast-enhanced abdominal ct. *Pattern recognition* 2009;42:1149-1161.

7.   Hoffman EA, Reinhardt JM, Sonka M, Simon BA, Guo J, Saba O, Chon D, Samrah S, Shikata H, Tschirren J, Palagyi K, Beck KC, McLennan G. Characterization of the interstitial lung diseases via density-based and texture-based analysis of computed tomography images of lung structure and function. *Academic radiology* 2003;10:1104-1118.

8.   Reilly J. Using computed tomographic scanning to advance understanding of chronic obstructive pulmonary disease. *Proceedings of the American Thoracic Society* 2006;3:450-455.

9.   Hoyert DL, Freedman MA, Strobino DM, Guyer B. Annual summary of vital statistics: 2000. *Pediatrics* 2001;108:1241-1255.

10.   Lozano R, Naghavi M, Foreman K, Lim S, Shibuya K, Aboyans V, Abraham J, Adair T, Aggarwal R, Ahn SY, Alvarado M, Anderson HR, Anderson LM, Andrews KG, Atkinson C, Baddour LM, Barker-Collo S, Bartels DH, Bell ML, Benjamin EJ, Bennett D, Bhalla K, Bikbov B, Bin Abdulhak A, Birbeck G, Blyth F, Bolliger I, Boufous S, Bucello C, Burch M, Burney P, Carapetis J, Chen H, Chou D, Chugh SS, Coffeng LE,

Colan SD, Colquhoun S, Colson KE, Condon J, Connor MD, Cooper LT, Corriere M, Cortinovis M, de Vaccaro KC, Couser W, Cowie BC, Criqui MH, Cross M, Dabhadkar KC, Dahodwala N, De Leo D, Degenhardt L, Delossantos A, Denenberg J, Des Jarlais DC, Dharmaratne SD, Dorsey ER, Driscoll T, Duber H, Ebel B, Erwin PJ, Espindola P, Ezzati M, Feigin V, Flaxman AD, Forouzanfar MH, Fowkes FG, Franklin R, Fransen M, Freeman MK, Gabriel SE, Gakidou E, Gaspari F, Gillum RF, Gonzalez-Medina D, Halasa YA, Haring D, Harrison JE, Havmoeller R, Hay RJ, Hoen B, Hotez PJ, Hoy D, Jacobsen KH, James SL, Jasrasaria R, Jayaraman S, Johns N, Karthikeyan G, Kassebaum N, Keren A, Khoo JP, Knowlton LM, Kobusingye O, Koranteng A, Krishnamurthi R, Lipnick M, Lipshultz SE, Ohno SL, Mabweijano J, MacIntyre MF, Mallinger L, March L, Marks GB, Marks R, Matsumori A, Matzopoulos R, Mayosi BM, McAnulty JH, McDermott MM, McGrath J, Mensah GA, Merriman TR, Michaud C, Miller M, Miller TR, Mock C, Mocumbi AO, Mokdad AA, Moran A, Mulholland K, Nair MN, Naldi L, Narayan KM, Nasseri K, Norman P, O'Donnell M, Omer SB, Ortblad K, Osborne R, Ozgediz D, Pahari B, Pandian JD, Rivero AP, Padilla RP, Perez-Ruiz F, Perico N, Phillips D, Pierce K, Pope CA, 3rd, Porrini E, Pourmalek F, Raju M, Ranganathan D, Rehm JT, Rein DB, Remuzzi G, Rivara FP, Roberts T, De Leon FR, Rosenfeld LC, Rushton L, Sacco RL, Salomon JA, Sampson U, Sanman E, Schwebel DC, Segui-Gomez M, Shepard DS, Singh D, Singleton J, Sliwa K, Smith E, Steer A, Taylor JA, Thomas B, Tleyjeh IM, Towbin JA, Truelsen T, Undurraga EA, Venketasubramanian N, Vijayakumar L, Vos T, Wagner GR, Wang M, Wang W, Watt K, Weinstock MA, Weintraub R, Wilkinson JD, Woolf AD, Wulf S, Yeh PH, Yip P, Zabetian A, Zheng ZJ, Lopez AD, Murray CJ, AlMazroa MA, Memish ZA. Global and regional mortality from 235 causes of death for 20 age groups in 1990 and 2010: A systematic analysis for the global burden of disease study 2010. *Lancet* 2012;380:2095-2128.

11.   National Heart L, and Blood Institute. Morbidity and mortality chart book. 2007.

12.   Mannino DM. Defining chronic obstructive pulmonary disease... And the elephant in the room. *The European respiratory journal : official journal of the European Society for Clinical Respiratory Physiology* 2007;30:189-190.

13.   Chapman KR, Mannino DM, Soriano JB, Vermeire PA, Buist AS, Thun MJ, Connell C, Jemal A, Lee TA, Miravitlles M, Aldington S, Beasley R. Epidemiology and costs of chronic obstructive pulmonary disease. *The European respiratory journal : official journal of the European Society for Clinical Respiratory Physiology* 2006;27:188-207.

14.   Friedlander AL, Lynch D, Dyar LA, Bowler RP. Phenotypes of chronic obstructive pulmonary disease. *Copd* 2007;4:355-384.

15.   Galban CJ, Han MK, Boes JL, Chughtai KA, Meyer CR, Johnson TD, Galban S, Rehemtulla A, Kazerooni EA, Martinez FJ, Ross BD. Computed tomography-based biomarker provides unique signature for diagnosis of copd phenotypes and disease progression. *Nature medicine* 2012;18:1711-1715.

16.   Zach JA, Newell JD, Jr., Schroeder J, Murphy JR, Curran-Everett D, Hoffman EA, Westgate PM, Han MK, Silverman EK, Crapo JD, Lynch DA, Investigators CO. Quantitative computed tomography of the lungs and airways in healthy nonsmoking adults. *Investigative radiology* 2012;47:596-602.

17.   Busacker A, Newell JD, Jr., Keefe T, Hoffman EA, Granroth JC, Castro M, Fain S, Wenzel S. A multivariate analysis of risk factors for the air-trapping asthmatic phenotype as measured by quantitative ct analysis. *Chest* 2009;135:48-56.

18.   Coxson HO, Mayo J, Lam S, Santyr G, Parraga G, Sin DD. New and current clinical imaging techniques to study chronic obstructive pulmonary disease. *American journal of respiratory and critical care medicine* 2009;180:588-597.

19.   Beckmann EC. Ct scanning the early days. *The British journal of radiology* 2006;79:5-8.

20.   Hu S, Hoffman EA, Reinhardt JM. Automatic lung segmentation for accurate quantitation of volumetric x-ray ct images. *IEEE Transactions on Medical Imaging* 2001;20:490-498.

21.   Zhang L, Hoffman EA, Reinhardt JM. Atlas-driven lung lobe segmentation in volumetric x-ray ct images. *IEEE Transactions on Medical Imaging* 2006;25:1-16.

22.   Wei Q, Hu Y, Gelfand G, Macgregor JH. Segmentation of lung lobes in high-resolution isotropic ct images. *IEEE transactions on bio-medical engineering* 2009;56:1383-1393.

23.   Sonka M, Park W, Hoffman EA. Rule-based detection of intrathoracic airway trees. *IEEE Transactions on Medical Imaging* 1996;15:314-326.

24.   Park W, Hoffman EA, Sonka M. Segmentation of intrathoracic airway trees: A fuzzy logic approach. *IEEE Transactions on Medical Imaging* 1998;17:489-497.

25.   Aykac D, Hoffman EA, McLennan G, Reinhardt JM. Segmentation and analysis of the human airway tree from three-dimensional x-ray ct images. *IEEE Transactions on Medical Imaging* 2003;22:940-950.

26.   Tschirren J, Hoffman EA, McLennan G, Sonka M. Segmentation and quantitative analysis of intrathoracic airway trees from computed tomography images. *Proceedings of the American Thoracic Society* 2005;2:484-487, 503-484.

27.   Tschirren J, Hoffman EA, McLennan G, Sonka M. Intrathoracic airway trees: Segmentation and airway morphology analysis from low-dose ct scans. *Medical Imaging, IEEE Transactions on* 2005;24:1529-1539.

28.   Shang Y, Deklerck R, Nyssen E, Markova A, de Mey J, Yang X, Sun K. Vascular active contour for vessel tree segmentation. *IEEE transactions on bio-medical engineering* 2011;58:1023-1032.

29.   Shikata H, McLennan G, Hoffman EA, Sonka M. Segmentation of pulmonary vascular trees from thoracic 3d ct images. *International journal of biomedical imaging* 2009;2009:636240.

30.   Washko GR, Lynch DA, Matsuoka S, Ross JC, Umeoka S, Diaz A, Sciurba FC, Hunninghake GM, San Jose Estepar R, Silverman EK, Rosas IO, Hatabu H. Identification of early interstitial lung disease in smokers from the copdgene study. *Academic radiology* 2010;17:48-53.

31.   Bakker ME, Putter H, Stolk J, Shaker SB, Piitulainen E, Russi EW, Stoel BC. Assessment of regional progression of pulmonary emphysema with ct densitometry. *Chest* 2008;134:931-937.

32.   Hatcher DC. Operational principles for cone-beam computed tomography. *Journal of the American Dental Association* 2010;141 Suppl 3:3S-6S.

33.   Flohr TG, Schaller S, Stierstorfer K, Bruder H, Ohnesorge BM, Schoepf UJ. Multi-detector row ct systems and image-reconstruction techniques. *Radiology* 2005;235:756-773.

34.   Hu H. Multi-slice helical ct: Scan and reconstruction. *Medical physics* 1999;26:5-18.

35.   Shope TB, Gagne RM, Johnson GC. A method for describing the doses delivered by transmission x-ray computed tomography. *Medical physics* 1981;8:488-495.

36.   Cameron JR, Zimmerman D, Kenney G, Buch R, Bland R, Grant R. Thermoluminescent radiation dosimetry utilizing lif. *Health physics* 1964;10:25-29.

37.   Suzuki A, Suzuki MN. Use of a pencil-shaped ionization chamber for measurement of exposure resulting from a computed tomography scan. *Medical physics* 1978;5:536-539.

38.   Jucius RA, Kambic GX. Measurements of computed tomography x-ray fields utilizing the partial volume effect. *Medical physics* 1980;7:379-382.

39.   Mountford PJ, Temperton DH. Recommendations of the international commission on radiological protection (icrp) 1990. *European journal of nuclear medicine* 1992;19:77-79.

40.   McCollough CH, Schueler BA. Calculation of effective dose. *Medical physics* 2000;27:828-837.

41.   Miyake H, et al. [medical electrical equipment - part 2-43: Particular requirements for the basic safety and essential performance of x-ray equipment for interventional procedures]. *Nihon Hoshasen Gijutsu Gakkai zasshi* 2011;67:298-301.

42.   Morin RL, Gerber TC, McCollough CH. Radiation dose in computed tomography of the heart. *Circulation* 2003;107:917-922.

43.   Primak AN, McCollough CH, Bruesewitz MR, Zhang J, Fletcher JG. Relationship between noise, dose, and pitch in cardiac multi-detector row ct. *Radiographics : a review publication of the Radiological Society of North America, Inc* 2006;26:1785-1794.

44.   Hounsfield GN. Computerized transverse axial scanning (tomography). 1. Description of system. *The British journal of radiology* 1973;46:1016-1022.

45.   Sun M, Nagy T, Virshup G, Partain L, Oelhafen M, Star-Lack J. Correction for patient table-induced scattered radiation in cone-beam computed tomography (cbct). *Medical physics* 2011;38:2058-2073.

46.   Siewerdsen JH, Jaffray DA. Cone-beam computed tomography with a flat-panel imager: Magnitude and effects of x-ray scatter. *Medical physics* 2001;28:220-231.

47.   Johnson TR, Krauss B, Sedlmair M, Grasruck M, Bruder H, Morhard D, Fink C, Weckbach S, Lenhard M, Schmidt B, Flohr T, Reiser MF, Becker CR. Material differentiation by dual energy ct: Initial experience. *European radiology* 2007;17:1510-1517.

48.   Hoffman EA. Effect of body orientation on regional lung expansion: A computed tomographic approach. *J Appl Physiol* 1985;59:468-480.

49.   Guo J, Fuld M, Alford SK, Reinhardt JM, Hoffman EA. Pulmonary analysis software suite 9.0 integrating quantitative measures of function with structural analyses. In M Brown, M de Bruijne, B van Ginneken, A Kiraly, J-M Kuhnigk, C Lorenz, K Mori, and J M Reinhardt, editors, First International Workshop on Pulmonary Image Analysis; 2008. p. 283-292.

50.   Guo J, Reinhardt J, Kitaoka H, Zhang L, Sonka M, McLennan G, Hoffman EA. Integrated system for ct-based assessment of parenchymal lung disease. *Biomedical Imaging, 2002 Proceedings 2002 IEEE International Symposium on* 2002:871-874.

51.   Simon BA. Non-invasive imaging of regional lung function using x-ray computed tomography. *Journal of Clinical Monitoring and Computing* 2000;16:433-442.

52.   Simon BA, Christensen GE, Low DA, Reinhardt JM. Computed tomography studies of lung mechanics. *Proceedings of the American Thoracic Society* 2005;2:517-521, 506-517.

53.   Badea CT, Guo X, Clark D, Johnston SM, Marshall CD, Piantadosi CA. Dual-energy micro-ct of the rodent lung. *American journal of physiology Lung cellular and molecular physiology* 2012;302:L1088-1097.

54.   Granton PV, Pollmann SI, Ford NL, Drangova M, Holdsworth DW. Implementation of dual- and triple-energy cone-beam micro-ct for postreconstruction material decomposition. *Medical physics* 2008;35:5030-5042.

55.   Nakayama Y, Awai K, Funama Y, Hatemura M, Imuta M, Nakaura T, Ryu D, Morishita S, Sultana S, Sato N, Yamashita Y. Abdominal ct with low tube voltage: Preliminary observations about radiation dose, contrast enhancement, image quality, and noise. *Radiology* 2005;237:945-951.

56.   Flohr TG, Klotz E, Allmendinger T, Raupach R, Bruder H, Schmidt B. Pushing the envelope: New computed tomography techniques for cardiothoracic imaging. *Journal of thoracic imaging* 2010;25:100-111.

57.   Kalender WA, Perman WH, Vetter JR, Klotz E. Evaluation of a prototype dual-energy computed tomographic apparatus. I. Phantom studies. *Medical physics* 1986;13:334-339.

58.   Brody WR, Cassel DM, Sommer FG, Lehmann LA, Macovski A, Alvarez RE, Pelc NJ, Riederer SJ, Hall AL. Dual-energy projection radiography: Initial clinical experience. *AJR American journal of roentgenology* 1981;137:201-205.

59.   Flohr TG, McCollough CH, Bruder H, Petersilka M, Gruber K, Suss C, Grasruck M, Stierstorfer K, Krauss B, Raupach R, Primak AN, Kuttner A, Achenbach S, Becker C, Kopp A, Ohnesorge BM. First performance evaluation of a dual-source ct (dsct) system. *European radiology* 2006;16:256-268.

60.   Johnson TR, Nikolaou K, Wintersperger BJ, Leber AW, von Ziegler F, Rist C, Buhmann S, Knez A, Reiser MF, Becker CR. Dual-source ct cardiac imaging: Initial experience. *European radiology* 2006;16:1409-1415.

61.   Flohr TG, Leng S, Yu L, Aiimendinger T, Bruder H, Petersilka M, Eusemann CD, Stierstorfer K, Schmidt B, McCollough CH. Dual-source spiral ct with pitch up to 3.2 and 75 ms temporal resolution: Image reconstruction and assessment of image quality. *Medical physics* 2009;36:5641-5653.

62.   Yu L, Primak AN, Liu X, McCollough CH. Image quality optimization and evaluation of linearly mixed images in dual-source, dual-energy ct. *Medical physics* 2009;36:1019.

63.   Primak AN, Giraldo JCR, Eusemann CD, Schmidt B, Kantor B, Fletcher JG, McCollough CH. Dual-source dual-energy ct with additional tin filtration: Dose and image quality evaluation in phantoms and in vivo. *American Journal of Roentgenology* 2010;195:1164-1174.

64.   Kyriakou Y, Kalender WA. Intensity distribution and impact of scatter for dual-source ct. *Phys Med Biol* 2007;52:6969-6989.

65.   Engel KJ, Herrmann C, Zeitler G. X-ray scattering in single-and dual-source ct. *Medical physics* 2008;35:318.

66.   Flohr TG, McCollough CH, Bruder H, Petersilka M, Gruber K, Süss C, Grasruck M, Stierstorfer K, Krauss B, Raupach R, Primak AN, Küttner A, Achenbach S, Becker C, Kopp A, Ohnesorge BM. First performance evaluation of a dual-source ct (dsct) system. *European radiology* 2006;16:256-268.

67.   Petersilka M, Stierstorfer K, Bruder H, Flohr T. Strategies for scatter correction in dual source ct. *Medical physics* 2010;37:5971-5992.

68.   Primak A. High resolution x-ray scattering studies of critical behavior at the nematic to smectic-a transition in a strong magnetic field. 2001.

69.   Matsuoka S, Yamashiro T, Washko GR, Kurihara Y, Nakajima Y, Hatabu H. Quantitative ct assessment of chronic obstructive pulmonary disease1. *Radiographics : a review publication of the Radiological Society of North America, Inc* 2010;30:55-66.

70.   Lynch DA. Quantitative ct of fibrotic interstitial lung disease. *Chest* 2007;131:643-644.

71.   Park E-A, Goo JM, Park SJ, Lee HJ, Lee CH, Park CM, Yoo C-G, Kim JH. Chronic obstructive pulmonary disease: Quantitative and visual ventilation pattern analysis at xenon ventilation ct performed by using a dual-energy technique. *Radiology* 2010;256:985-997.

72.   Lynch DA, Newell JD. Quantitative imaging of copd. *Journal of thoracic imaging* 2009;24:189-194.

73.   Team NLSTR, Aberle DR, Berg CD, Black WC, Church TR, Fagerstrom RM, Galen B, Gareen IF, Gatsonis C, Goldin JG, Gohagan JK, Hillman B, Jaffe C, Kramer BS, Lynch D, Marcus PM, Schnall M, Sullivan DC, Sullivan D, Zylak CJ. The national lung screening trial: Overview and study design. *Radiology* 2011;258:243-253.

74.   Kim WJ, Hoffman EA, Reilly J, Hersh C, Demeo D, Washko G, Silverman EK. Association of copd candidate genes with computed tomography emphysema and airway phenotypes in severe copd. *The European respiratory journal : official journal of the European Society for Clinical Respiratory Physiology* 2011;37:39-43.

75.   Bakker ME, Stolk J, Putter H, Shaker SB, Parr DG, Piitulainen E, Russi EW, Dirksen A, Stockley RA, Reiber JH, Stoel BC. Variability in densitometric assessment of pulmonary emphysema with computed tomography. *Investigative radiology* 2005;40:777-783.

76.   Bankier AA, De Maertelaer V, Keyzer C, Gevenois PA. Pulmonary emphysema: Subjective visual grading versus objective quantification with macroscopic morphometry and thin-section ct densitometry. *Radiology* 1999;211:851-858.

77.   Gurney JW, Jones KK, Robbins RA, Gossman GL, Nelson KJ, Daughton D, Spurzem JR, Rennard SI. Regional distribution of emphysema: Correlation of high-resolution ct with pulmonary function tests in unselected smokers. *Radiology* 1992;183:457-463.

78.   Lucidarme O, Coche E, Cluzel P, Mourey-Gerosa I, Howarth N, Grenier P. Expiratory ct scans for chronic airway disease: Correlation with pulmonary function test results. *AJR American journal of roentgenology* 1998;170:301-307.

79.   Knudson RJ, Standen JR, Kaltenborn WT, Knudson DE, Rehm K, Habib MP, Newell JD. Expiratory computed tomography for assessment of suspected pulmonary emphysema. *Chest* 1991;99:1357-1366.

80.   Brown M, Abtin F, Kim HJ, McNitt-Gray M, Goldin JG. Imaging biomarkers for patient selection and treatment planning in emphysema. *Imaging in Medicine* 2010;2:565-573.

81.   Buckler AJ, Mozley PD, Schwartz L, Petrick N, McNitt-Gray M, Fenimore C, O'Donnell K, Hayes W, Kim HJ, Clarke L, Sullivan D. Volumetric ct in lung cancer: An example for the qualification of imaging as a biomarker.; 2010.

82.   Bafadhel M, Umar I, Gupta S, Raj JV, Vara DD, Entwisle JJ, Pavord ID, Brightling CE, Siddiqui S. The role of ct scanning in multidimensional phenotyping of copd. *Chest* 2011;140:634-642.

83.   Goldin JG. Imaging the lungs in patients with pulmonary emphysema. *Journal of thoracic imaging* 2009;24:163-170.

84.   Newell JD. Quantitative computed tomography of lung parenchyma in chronic obstructive pulmonary disease: An overview. *Proceedings of the American Thoracic Society* 2008;5:915-918.

85.   Coxson HO, Rogers Robert M. Quantitative computed tomography of chronic obstructive pulmonary disease. *Academic radiology* 2005;12:1457-1463.

86.   Newell JD, Jr., Hogg JC, Snider GL. Report of a workshop: Quantitative computed tomography scanning in longitudinal studies of emphysema. *The European respiratory journal : official journal of the European Society for Clinical Respiratory Physiology* 2004;23:769-775.

87.   Stolk J, Ng WH, Bakker ME, Reiber JH, Rabe KF, Putter H, Stoel BC. Correlation between annual change in health status and computer tomography derived lung density in subjects with alpha1-antitrypsin deficiency. *Thorax* 2003;58:1027-1030.

88.   Coxson HO. Quantitative computed tomography assessment of airway wall dimensions: Current status and potential applications for phenotyping chronic obstructive pulmonary disease. *Proceedings of the American Thoracic Society* 2008;5:940-945.

89.   Hoffman EA, Simon BA, McLennan G. A structural and functional assessment of the lung via multidetector-row computed tomography : Phenotyping chronic obstructive pulmonary disease. *Proceedings of the American Thoracic Society* 2006;3:519-534.

90.   Dirksen A, Piitulainen E, Parr DG, Deng C, Wencker M, Shaker SB, Stockley RA. Exploring the role of ct densitometry: A randomised study of augmentation therapy in alpha1-antitrypsin deficiency. *The European respiratory journal : official journal of the European Society for Clinical Respiratory Physiology* 2009;33:1345-1353.

91.   Sieren JP, Gunderson K, Lynch DA, Newell JD, Judy P, Hoffman EA. Copdgene phantom: Quality control of quantitative lung imaging in a multi-center trial. *American journal of respiratory and critical care medicine* 2010;181:A5519.

92.   Bruder H, Stierstorfer K, Petersilka M, Wiegand C, Suess C, Flohr T. Correction of cross-scatter in next generation dual source ct (dsct) scanners. 2008;6913:69131W-69131W-69110.

93.   Ohnesorge B, Flohr T, Klingenbeck-Regn K. Efficient object scatter correction algorithm for third and fourth generation ct scanners. *European radiology* 1999;9:563-569.

94.   Zhu L, Bennett NR, Fahrig R. Scatter correction method for x-ray ct using primary modulation: Theory and preliminary results. *IEEE Trans Med Imaging* 2006;25:1573-1587.

95.   Siewerdsen JH, Daly MJ, Bakhtiar B, Moseley DJ, Richard S, Keller H, Jaffray DA. A simple, direct method for x-ray scatter estimation and correction in digital radiography and cone-beam ct. *Medical physics* 2006;33:187-197.

96.   Schindera ST, Tock I, Marin D, Nelson RC, Raupach R, Hagemeister M, von Allmen G, Vock P, Szucs-Farkas Z. Effect of beam hardening on arterial enhancement in thoracoabdominal ct angiography with increasing patient size: An in vitro and in vivo study. *Radiology* 2010;256:528-535.

97.   Barnes PJ, Chowdhury B, Kharitonov SA, Magnussen H, Page CP, Postma D, Saetta M. Pulmonary biomarkers in chronic obstructive pulmonary disease. *American journal of respiratory and critical care medicine* 2006;174:6-14.

98.   Schuster DP. The opportunities and challenges of developing imaging biomarkers to study lung function and disease. *American journal of respiratory and critical care medicine* 2007;176:224-230.

99.   Parr DG, Stoel BC, Stolk J, Nightingale PG, Stockley RA. Influence of calibration on densitometric studies of emphysema progression using computed tomography. *American journal of respiratory and critical care medicine* 2004;170:883-890.

100.   Patel BD, Coxson HO, Pillai SG, Agusti AG, Calverley PM, Donner CF, Make BJ, Muller NL, Rennard SI, Vestbo J, Wouters EF, Hiorns MP, Nakano Y, Camp PG, Nasute Fauerbach PV, Screaton NJ, Campbell EJ, Anderson WH, Pare PD, Levy RD, Lake SL, Silverman EK, Lomas DA, International CGN. Airway wall thickening and emphysema show independent familial aggregation in chronic obstructive pulmonary disease. *American journal of respiratory and critical care medicine* 2008;178:500-505.

101.   King GG, Muller NL, Pare PD. Evaluation of airways in obstructive pulmonary disease using high-resolution computed tomography. *American journal of respiratory and critical care medicine* 1999;159:992-1004.

102.   Nakano Y, Muller NL, King GG, Niimi A, Kalloger SE, Mishima M, Pare PD. Quantitative assessment of airway remodeling using high-resolution ct. *Chest* 2002;122:271S-275S.

103.   Nakano Y, Wong JC, de Jong PA, Buzatu L, Nagao T, Coxson HO, Elliott WM, Hogg JC, Pare PD. The prediction of small airway dimensions using computed tomography. *American journal of respiratory and critical care medicine* 2005;171:142-146.

104.   Hogg JC, Chu F, Utokaparch S, Woods R, Elliott WM, Buzatu L, Cherniack RM, Rogers RM, Sciurba FC, Coxson HO, Pare PD. The nature of small-airway obstruction in chronic obstructive pulmonary disease. *The New England journal of medicine* 2004;350:2645-2653.

105.   Achenbach T, Weinheimer O, Dueber C, Heussel CP. Influence of pixel size on quantification of airway wall thickness in computed tomography. *Journal of computer assisted tomography* 2009;33:725-730.

106.   Madani A, De Maertelaer V, Zanen J, Gevenois PA. Pulmonary emphysema: Radiation dose and section thickness at multidetector ct quantification--comparison with macroscopic and microscopic morphometry. *Radiology* 2007;243:250-257.

107.   Lee CH, Goo JM, Ye HJ, Ye SJ, Park CM, Chun EJ, Im JG. Radiation dose modulation techniques in the multidetector ct era: From basics to practice. *Radiographics : a review publication of the Radiological Society of North America, Inc* 2008;28:1451-1459.

108.   Remy-Jardin M, Faivre J-B, Pontana F, Hachulla A-L, Tacelli N, Santangelo T, Remy J. Thoracic applications of dual energy. *Radiologic Clinics of North America* 2010;48:193-205.

109.   Ko JP, Brandman S, Stember J, Naidich DP. Dual-energy computed tomography: Concepts, performance, and thoracic applications. *Journal of thoracic imaging* 2012;27:7-22.

110.   Lee CW, Seo JB, Lee Y, Chae EJ, Kim N, Lee HJ, Hwang HJ, Lim CH. A pilot trial on pulmonary emphysema quantification and perfusion mapping in a single-step

using contrast-enhanced dual-energy computed tomography. *Investigative radiology* 2011.